Extreme ^{13}C-depletions and organic sulfur content argue for S-fueled anaerobic methane oxidation in 2.72 Ga old stromatolites

Kevin Lepot [a, b,*], Kenneth H. Williford [b, c], Pascal Philippot [d, e], Christophe Thomazo [f], Takayuki Ushikubo [b, g], Kouki Kitajima [b], Smaïl Mostefaoui [h], John W. Valley [b]

[a] *Université de Lille, CNRS, Université Littoral Côte d'Opale, UMR 8187 Laboratoire d'Océanologie et de Géosciences, 59000 Lille, France*

[b] *NASA Astrobiology Institute, WiscSIMS, Department of Geoscience, University of Wisconsin, Madison, WI 53706, USA*

[c] *Jet Propulsion Laboratory, California Institute of Technology, Pasadena, CA 91109, USA*

[d] *Géosciences Montpellier, CNRS-UMR 5243, Université de Montpellier, 34000 Montpellier, France*

[e] *Institut de Physique du Globe—Sorbonne Paris Cité, Université Paris Diderot, CNRS UMR7154, 75238 Paris, France*

[f] *Université Bourgogne Franche-Comté UMR CNRS 6282, Biogéosciences, 21000 Dijon, France*

[g] *Kochi Institute for Core Sample Research, JAMSTEC, Nankoku, Kochi 783-8502, Japan*

[h] *Institut de Minéralogie, de Physique des Matériaux, et de Cosmochimie, UMR CNRS 7590, UMR IRD 206, Sorbonne Universités - Muséum National d'Histoire Naturelle, 75231 Paris, France*

** Corresponding author contact: kevin.lepot@univ-lille.fr; +33320434921*

LINK TO PUBLISHED VERSION

including supplementary data to this article:

https://doi.org/10.1016/j.gca.2018.10.014

Keywords: Early life; SIMS; Carbon isotopes; Organic matter; Stromatolites; Sulfurization, Tumbiana Formation; Methanotrophy

Abbreviations: Acetyl-CoA: acetyl-coenzyme A. ANME: anaerobic methanotroph. AOM: anaerobic oxidation of methane. EDXS: energy-dispersive X-ray spectrometry. Ga: giga-annum. MIF-S: mass independent fractionation of sulfur isotopes. MSR: microbial sulfate reduction/reducers. OM: organic matter. SEM: scanning electron microscopy. SD: standard deviation. SE: standard error. SIMS: secondary ion mass spectrometry. STXM: scanning transmission X-ray microscopy. XANES: X-ray absorption near-edge structure.

Abstract

The extreme ^{13}C-depletions recorded in Neoarchean organic matter (OM) have commonly been interpreted as markers of methanotrophy. This methane oxidation metabolism could have been performed using oxidants such as dioxygen, sulfate, nitrite/nitrate, and/or Fe^{3+}- and Mn^{4+}-minerals. Acetogenesis using acetyl-CoA metabolism may produce similar ^{13}C-depletions. We investigated $\delta^{13}C$ and S/C values of OM in 2.72 Ga old lacustrine stromatolites of the Tumbiana Formation (Australia) using Secondary Ion Mass Spectrometry (SIMS), coupled with X-ray spectroscopy. Type-A OM is embedded in quartz and/or chlorite. We show that mixtures of chlorite bias negatively the $\delta^{13}C_{org}$ of associated OM measured by SIMS, likely through recombination of hydrogen from chlorite with carbon from OM during analysis. Type-A OM, associated with quartz or interleaved with chlorites (but remote enough to avoid H-recombination), displays $\delta^{13}C_{org}$ between –56.1 and –50.6 ‰ VPDB (mean: –53.5 ‰, SD ±1.8 ‰). The intimate association of Type-A OM with Fe-rich chlorite and its main occurrence in pyritic layers coupled with ^{13}C-depletions is most parsimoniously interpreted as anaerobic methanotrophy using Fe^{3+}-minerals and/or oxidized S. Type-B OM comprises <2-µm organic globules embedded in calcite. A mass balance correction using the $\delta^{13}C$ values measured on Type-B globules mixed with calcite and those measured on pure calcite yielded corrected $\delta^{13}C^*_{org}$ values for the globules ranging between –65.2 and –52.5 ‰ (mean –58.8 ‰, SD ±3.6 ‰). In a context where Fe and S reduction could outcompete acetogenesis for a fraction of any available H_2, these extremely low $\delta^{13}C_{org}$ values are difficult to explain with chemoautotrophic acetogenesis. Atomic S/C ratios in Type-B globules reach up to 0.042, i.e. up to tenfold the values (0.003–0.004) in Type A-OM. These organic S concentrations, combined with the extremely low $\delta^{13}C^*_{org}$ values, support anaerobic oxidation of methane coupled to sulfur oxidation. Finally, Type-C OM, interpreted as migrated pyrobitumen nodules, displays $\delta^{13}C_{org}$ of –48 to –39.1 ‰. The most extreme low-$\delta^{13}C_{org}$ values of the Precambrian are thus best interpreted as the result of lacustrine methanotrophy fueled by oxidized S and/or Fe species, which likely derived from oxygenic and/or anoxygenic photosynthesis. Photosynthesis, followed by methanogenesis and methanotrophy may have been important in lakes at a time of supercontinent growth and eruption of large subaerial igneous provinces. In this context, anaerobic methanotrophy could have played a part in regulating atmospheric methane.

1. Introduction

The low O_2 concentration of the Archean atmosphere is indicated by mass independent fractionation of sulfur isotopes (MIF-S[1], Farquhar et al., 2000; Pavlov and Kasting, 2002), which only disappeared after the Great Oxygenation Event, ca. 2.45–2.31 Ga ago (Guo et al., 2009; Luo et al., 2016; Philippot et al., 2018). The Neoarchean (ca. 2.8–2.5 Ga) has been distinguished from the earlier Archean by increase in MIF-S magnitude from $|\Delta^{33}S|<3‰$ between 3.2 and ca. 2.71 Ga to >3‰ and a change in the slope of $\Delta^{36}S/\Delta^{33}S$ from -1.5 to -0.9 at ca. 2.71 Ga (Kurzweil et al., 2013). These changes have been interpreted as the result of increased biological oxygen and methane production (Kurzweil et al., 2013). Indeed, O_2 production is proposed as early as 3.0–2.8 Ga ago based on Cr isotope ratios (Frei et al., 2009; Crowe et al., 2013), 2.95 Ga based on Mo isotope ratios (Planavsky et al., 2014), 2.5 Ga based on Mo and Re abundance (Anbar et al., 2007), on N isotope ratios (Garvin et al., 2009), and on Se isotope ratios (Stüeken et al., 2015a). Moreover, the pronounced increase in abundance and diversity of stromatolitic carbonates also suggests a change in the evolution of the biosphere during the Neoarchean (Hofmann, 2000). The accretion of stromatolites could derive (indirectly: Dupraz *et al.*, 2009) from various autotrophic metabolisms such as oxygenic and anoxygenic photosynthesis (Fig. 1A; Bosak et al., 2013) or via anaerobic oxidation of methane (AOM) (Greinert et al., 2002). Some Neoarchean stromatolites display fabrics strongly suggesting they formed in presence of photosynthetic bacteria. These fabrics include tufted mats similar to those formed by cyanobacteria (Flannery and Walter, 2012), clumps similar to those formed by filamentous cyanobacteria in response to O_2 (Sim et al., 2012), and palisade textures similar to those formed by vertically erected phototropic filaments (Buick, 1992).

The Fortescue Group of Western Australia records the largest negative excursion—the "Fortescue excursion"— in the organic carbon isotope ($\delta^{13}C_{org}$[1]) record, with $\delta^{13}C_{org}$ values as low as -60.9 ‰ (reviews of the data in Thomazo et al., 2009a; Flannery et al., 2016). These extreme ^{13}C-depletions, as well as other values lower than ca. -40 ‰ commonly recorded in other Neoarchean rocks have been interpreted to be the result of methanotrophy (i.e. the oxidation of methane by prokaryotes)

[1] Isotope ratios are given as δ deviations—in permil (‰) units—of the ratio of the isotope compositions of mass X to mass Y relative to the same ratio in a reference standard. The international reference standards are VPDB (Vienna Pee Dee Belemnite) for C isotopes, VCDT (Vienna Canyon Diablo Troilite) for S isotopes, and IRMM-014 for Fe isotopes. Deviations for S-, C and Fe-isotopes ratios reported or discussed here are calculated using: $\delta^{M}S = 1000*[(^{M}S/^{32}S)_{sample} - (^{M}S/^{32}S)_{VCDT}]/(^{M}S/^{32}S)_{VCDT}$ with M=33, 34 or 36, $\delta^{13}C = 1000*[(^{13}C/^{12}C)_{sample} - (^{13}C/^{12}C)_{VPDB}]/(^{13}C/^{12}C)_{VPDB,}$ and $\delta^{56}Fe = 1000*[(^{56}Fe/^{54}Fe)_{sample} - (^{56}Fe/^{54}Fe)_{IRMM-014}]/(^{56}Fe/^{54}Fe)_{IRMM-014}$. Mass-independent fractionations of S isotopes (MIF-S) are defined as non-zero values of the capital-delta deviations $\Delta^{33}S = \delta^{33}S - 1000*[(1+ \delta^{34}S/1000)^{0.515}–1]$ and $\Delta^{36}S = \delta^{36}S - 1000*[(1+ \delta^{34}S/1000)^{1.9}–1]$.

(Schoell and Wellmer, 1981; Hayes, 1994). Methanotrophy could have been performed aerobically ($CH_4 + 2O_2 \rightarrow CO_2 + 2H_2O$, Fig. 1J) using photosynthetically produced O_2 (Hayes, 1994). Molecules of 3-methylhopane found in Neoarchean rocks suggest aerobic methanotrophs (Eigenbrode et al., 2008), although these molecules may have been produced by other bacteria (Welander and Summons, 2012). Moreover, the lack of these molecules in new samples from the same stratigraphic intervals recovered by ultraclean drilling methods shows that previously reported Archean biomarkers from Western Australia were the result of contamination during conventional drilling or curation (French et al., 2015). Alternatively, methanotrophy could have been performed anaerobically (AOM, Fig. 1K-L) using other oxidants such as sulfate, nitrite/nitrate, Fe^{3+}-minerals, or Mn^{4+}-minerals (Raghoebarsing et al., 2006; Beal et al., 2009; Knittel and Boetius, 2009). Today's most common AOM pathway uses sulfate ($CH_4 + SO_4^{2-} \rightarrow HCO_3^- + HS^- + H_2O$) and, by extension, may explain the Fortescue $\delta^{13}C_{org}$ excursion (Hinrichs, 2002). The sulfate fueling this type of AOM could have been produced through photolytic dissociation of SO_2 in an anoxic atmosphere (Farquhar et al., 2001) and/or chemotrophic or phototrophic S-oxidizing bacteria (Konhauser, 2007; Ghosh and Dam, 2009). Isotope fractionations indicative of microbial sulfate reduction (MSR, Fig. 1D, 1G) are indicated at ca. 3.5 Ga (Philippot *et al.*, 2007; Ueno *et al.*, 2008; Shen *et al.*, 2001, 2009), 2.7 Ga (Thomazo et al., 2013), and 2.5 Ga (Zhelezinskaia et al., 2014). Bulk-rock $\delta^{34}S$ values of pyrite between 2.7 and 3 Ga display a small range of values of ca. 0 ±8 ‰ (Thomazo et al., 2009a; Thomazo et al., 2009b; Johnston, 2011), with one exception in the 2.7 Ga Manjeri Formation, Zimbabwe (Grassineau et al., 2002; Thomazo et al., 2013). This small range is indistinguishable from the range of values produced during abiotic processes (such as thermochemical sulfate reduction, e.g. Watanabe et al., 2009) but is nevertheless consistent with small fractionations produced during MSR under low sulfate concentrations (Habicht et al. 2002) or mixing with sulfide derived (abiotically) from elemental S (Farquhar et al., 2013). In contrast, large ranges of positive and negative $\delta^{34}S$ recorded at the microscale indicate MSR in lacustrine stromatolites of the Fortescue Group (Tumbiana Formation, Marin-Carbonne et al., 2018) and younger Neoarchean rocks (Kamber and Whitehouse, 2006; Farquhar et al., 2013; Fischer et al., 2014) and show that sulfate was abundant enough to express S-isotope fractionations. Sulfate concentrations of less than 2.5 micromolar have been suggested for Archean seawater (Crowe et al., 2014). Such low concentrations have been proposed to limit AOM (Slotznick and Fischer, 2016). However, sulfate-dependent AOM has been shown to proceed at high rates even at such low concentrations (Beal et al., 2011). In modern sediments, AOM can reduce Fe^{3+}-minerals in addition to, or instead of, sulfate (Sivan et al., 2014; Egger et al., 2016; Bar-Or et al., 2017). Minerals rich in Fe^{3+} could have been produced throughout the Archean as the result of oxygenic and/or anoxygenic photosynthesis (Fig. 1A), as suggested by Fe-isotopes (Yoshiya et al., 2012; Li et al., 2013; Dauphas et al., 2017; Busigny et al., 2017). The coupling of ^{13}C-depleted kerogen and highly negative $\delta^{56}Fe$ has been used to suggest AOM was coupled to microbial Fe-reduction during the deposition of the Fortescue Group (Yoshiya et al., 2012).

It has been proposed that Neoarchean methanotrophy was not compatible with the textures and isotopic composition of the carbonates associated with ^{13}C-depleted kerogen (Slotznick and Fischer, 2016), although this argument has been refuted (Flannery *et al.*, 2016; Stüeken *et al.*, 2017, see also section 5.3). As an alternative to methanotrophy, extreme ^{13}C-depletions in OM could result from

chemotrophic metabolisms using the acetyl-CoA (Wood-Ljungdahl) pathway (Slotznick and Fischer, 2016), e.g. Fig. 1C. One of the most controversial aspects of this model is that it allows formation of strongly ^{13}C-depleted kerogen without the need of cycling primary photosynthetic biomass through fermentation, methanogenesis and methanotrophy (Slotznick and Fischer, 2016), supporting the hypothesis that oxygenic photosynthesis appeared much later during the late Archean or Paleoproterozoic (Kopp et al., 2005; Fischer et al., 2016).

It has been suggested that high concentrations of atmospheric methane could have led to the formation of organic aerosols with $\delta^{13}C_{org}$ values as low as -65 ‰ without methanotrophic metabolism (Pavlov et al., 2001). However, the ^{13}C-depletions are more prominent in mudstones compared to stromatolites and silts at the same locality (Thomazo et al., 2009b), in lakes with a basaltic rather than felsic catchment (Stüeken et al., 2017), and in lacustrine and shallow marine compared to open marine deposits (Eigenbrode and Freeman, 2006; Flannery et al., 2016). These spatial heterogeneities support a local (i.e. sedimentary) rather than global (i.e. atmospheric) control on $\delta^{13}C_{org}$ (Thomazo et al., 2009b; Flannery et al., 2016). The apparent relationship between the larger $\Delta^{33}S$ and the lowest $\delta^{13}C_{org}$ in the 2.72 Ga Tumbiana Formation is also consistent with the hypothesis of methanotrophy under an atmosphere poor in organic aerosols (Thomazo et al., 2009b). Periodic changes in slope of $\Delta^{36}S/\Delta^{33}S$ to values less than -1 linked with lower $\delta^{13}C_{org}$ values after 2.71 Ga have been interpreted as the result of periodic organic aerosol haze caused by increased methanogenesis (Zerkle et al., 2012; Izon et al., 2015; Williford et al., 2016; Izon et al., 2017), possibly concomitant with increased oxygenic photosynthesis (Kurzweil et al., 2013). This link is, however, not apparent in all >2.71 Ga units, possibly as the result of methanotrophy preventing organic haze formation (Thomazo et al., 2009b; Thomazo et al., 2013) or of variable effects of organic haze on $\Delta^{36}S/\Delta^{33}S$ (Izon et al., 2017). A better understanding of the origin of the extreme $\delta^{13}C_{org}$ fractionations recorded during the Neoarchean could help tie microbial metabolism and the evolution of atmospheric chemistry during the prologue to atmospheric oxygenation.

Here, we investigate the organic matter (OM) from two lacustrine stromatolites of the Tumbiana Formation of the Fortescue Group, Western Australia, using a combination of X-ray spectroscopies, microscale analysis of organic carbon isotopes using Secondary Ion Mass Spectrometry (SIMS) and nanoanalyses of S/C with NanoSIMS. We document three distinct types of OM recognizable by their C-isotope compositions, petrographic contexts, and organic sulfur contents. Type-C OM is interpreted as migrated pyrobitumen and displays the highest $\delta^{13}C$ values. Pronounced enrichments in organic sulfur are only found in Type-B OM, which displays the lowest $\delta^{13}C_{org}$ values. We interpret this C-S relationship to reflect the operation of sulfur-dependent AOM. Type-A OM is poor in organic S but associated with Fe-minerals. This OM type is most parsimoniously interpreted as the product of sulfate- and/or Fe-dependent AOM.

2. Geological context and drillcores

The Tumbiana Formation is part of the Fortescue Group (Western Australia), which deposited over the granitoid-greenstone basement of the Pilbara Craton and which is overlain by the Hamersley Group (Thorne and Trendall, 2001), Fig. 2. The Tumbiana Formation has been dated at 2724 ± 5 Ma using zircon U-Pb ages (Blake et al., 2004). The lower part of the Tumbiana Formation is the Mingah Member, which features both primary and reworked mafic tuffs (Lepot et al., 2011). This unit is overlain by the Meentheena Member, which comprises a suite of mudstones, siltstones, carbonate stromatolites and carbonate sandstones. Stromatolitic horizons of the Meentheena Member are 0.5- to 20-m thick and can be followed along strike for several kilometers (Thorne and Trendall, 2001). The Tumbiana Formation is overlain by subaerial basalts of the Maddina Formation.

The Fortescue Group experienced regional low-grade metamorphism (Smith et al., 1982) at about 2.2 Ga (Rasmussen et al., 2001). The studied rocks come from the Meentheena locality (Thorne and Trendall, 2001; Lepot et al., 2009a) in the metamorphism zone (II) of Smith et al. (1982) shown in Fig. 2, which displays prehnite-pumpellyite facies with epidote. This metamorphic grade/facies together with the maturity of organic matter inferred with Raman spectroscopy indicate metamorphism temperatures no higher than 300°C (Lepot et al., 2008). Regional metamorphism of the Fortescue Group was locally followed–as indicated by petrographic relationships–by heterogeneous metasomatism leading to transformation of primary volcanic minerals and clays (such as chlorite) into epidote (White et al., 2014), which was not observed in the basaltic flow overlying the studied sedimentary rocks.

Sediment facies and trace element compositions support deposition of the Meentheena Member stromatolites in a giant lake system (Buick, 1992; Bolhar and Van Kranendonk, 2007; Awramik and Buchheim, 2009; Coffey et al., 2013). Shallow marine deposition has also been proposed for some parts of the Meentheena Member (Thorne and Trendall, 2001; Sakurai et al., 2005), in particular based on herringbone cross-bedding at the Redmont/Knossos locality (Sakurai et al., 2005), but these could not be found by subsequent studies and have been re-interpreted as trough cross-bedding (Awramik and Buchheim, 2009; Coffey et al., 2013; Flannery et al., 2016).

Here we study samples of the PDP1 drill core recovered from the Meentheena locality at 21°18'15"S and 120°24'40"E (Philippot et al., 2009; Van Kranendonk et al., 2006, Fig. 2). The top 42.7 m of the core comprise metabasalts of the Maddina Formation. The Meentheena Member of the Tumbiana Formation was intersected between 42.7 and ~92m, followed by the Mingah Member until core end at 104 m (Philippot et al., 2009). This study focuses on the two stromatolite samples described in Lepot *et al.* (2009a) and whose bulk chemistry is described in Thomazo *et al.* (2009b, 2011). Our thin sections KGI68.2 and KGI68.2' come from the same core depth (68.2 m), and the thin section 69.2a comes from 1 m deeper. These samples come from below the modern water table and appeared pristine of recent meteoric alteration (Lepot et al., 2008). Nano-pyrites with $\delta^{34}S$ values from -33.7 to +64.4 ‰ indicate MSR in individual microscopic layers of organic matter enclosed in a domical stromatolite from 68.9 m in the same drillcore (Marin-Carbonne et al., 2018). Arsenic enrichments in specific layers of the stromatolite sample from 69.7 m core depth suggest that arsenite might have been oxidized by microorganisms and in turn might have been available for chemoautotrophic and/or heterotrophic aresenate reducers (Sforna et al., 2014; Sforna et al., 2017).

3. Methods

3.1. Scanning Transmission X-ray Microscopy

Scanning transmission X-ray microscopy (STXM) was used to perform X-ray Absorption Near-edge spectroscopy (XANES) at the sulfur L-edge (in the energy range 155–190 eV) to evaluate the speciation of sulfur atoms. Ultrathin sections (~140 nm) were prepared for STXM using Focused ion beam milling (Lepot et al., 2009a). Beamline 10ID-1 (SM beamline) of the Canadian Light Source synchrotron (Kaznatcheev et al., 2007) was used to perform STXM. The instrument chamber was pumped down to 100 mTorr and filled with He prior to analyses. Sulfur L-edge XANES spectra were extracted from hyperspectral stacks of energy-filtered images (Jacobsen et al., 2000) recorded with a spectral resolution of 0.5 eV between 155–161 eV, 0.15 eV between 161–175 eV, and 0.5 eV between 175–190 eV. The spatial resolution was about 25 nm and counting times were a few milliseconds or less per pixel. Data were processed using AXis2000 (hyperspectral data reconstruction and spatial shift alignment), available on http://unicorn.mcmaster.ca/aXis2000.html.

3.2. Sample preparation and SEM

Samples were prepared for SEM and SIMS as detailed in Lepot et al. (2013). In brief, doubly polished thin sections ca. 100-µm-thick were unglued in acetone and broken into millimetric fragments. The later were deposited face-down onto double-sided tape and embedded in epoxy mounts (i.e. epoxy did not flow on the surface of interest in contact with tape). The surface of each mount was polished with Al_2O_3 suspensions and mounts were cleaned in ethanol. Targets were located with optical microscopy in reflected and transmitted light. After coating mounts with 5 nm of gold, SEM was used to image the targets prior to SIMS. Secondary and backscattered electron images and EDXS (Energy Dispersive X-ray Spectrometer) elemental maps were recorded using a Thermo Electron detector on a Hitachi S3400 SEM (at University of Wisconsin - Madison) at a working distance of 10 mm and 10 kV (EDXS spectra/maps) or 15 kV (imaging). Using EDXS spectra, an approximation of relative variations in S/C in OM (henceforth termed "S/C proxy") was derived from the ratios of the heights of single peaks (pulses) at 0.27 (carbon) and 2.33 (sulfur) keV. The "S/C proxy" is proportional to true S/C concentrations but true quantification cannot be made because quantification of organic C is not possible using EDXS due to large bias on light elements. Additional SEM analyses were performed using a FEI Quanta 200 SEM equipped with a Bruker Quantax EDXS (at Université de Lille). The SEM operated at a working distance of 10 mm and 10 kV (EDXS spectra) or 20 kV (EDXS maps, imaging). After SIMS analyses, SEM was performed after removal (polishing) of the 35 nm gold coating used for SIMS, and deposition of ~5 nm of gold, which leaves remains of the thicker gold coating in the topographic lows.

3.3. NanoSIMS

Quantitative imaging of ^{12}C and ^{32}S was performed using a NanoSIMS 50 at MNHN, IMPMC laboratory, Paris. Stacks of ion images of $^{12}C^-$, $^{28}Si^-$ and $^{32}S^-$ were obtained by rastering a Cs^+ beam of ~150 nm as detailed in Supplementary Table 1. OpenMIMS v3.0.4 (National Resource for Imaging Mass Spectrometry) was used to align automatically the image stacks, apply a 44 nanosecond electron-multiplier dead-time correction, and extract $^{12}C^-$ and $^{32}S^-$ counts in regions of interest of the quantitative image stacks. Regions of interest were drawn to avoid nanopyrites with intense S signal and weak C signal. Since elements present different ionization efficiencies during NanoSIMS analysis, standard analysis is required to determine relative sensitivity factors to derive $^{32}S/^{12}C$ ratios from measured $^{32}S^-/^{12}C^-$ intensity ratios. The LGIS-A1 anthracite standard

(Supplementary Table 2) was used to yield atomic S/C ratios. External precision of two standard deviations (2SD) of three analyses of LGIS-A1 yielded 1.14×10^{-4} on the atomic S/C. Internal precision on the atomic S/C is reported as two standard errors (2SE) calculated from multiple measurement cycles within each analysis. Internal precision is an order of magnitude higher than external precision, and henceforth only the former is reported. We note that a more accurate quantification of S/C could be made using a set of standards with variable S/C (see Thomen *et al.*, 2014 for N/C).

3.4. SIMS

Secondary ion mass spectrometry analyses of carbon isotope ratios were carried out using a CAMECA IMS 1280 at the WiscSIMS laboratory, University of Wisconsin-Madison (Valley and Kita, 2009) during three different sessions. In general, we followed techniques described previously (Williford et al., 2016), and specific analytical parameters for the three different sessions are given in Supplementary Table 1. About 30 nm of gold coating was added after SEM imaging and samples were degassed for 48 h at 10^{-9} torr in the SIMS sample chamber prior to analysis. A primary focused beam of $^{133}Cs^+$ was used to sputter superficial zones ca. 6 µm, 3 µm and 1 µm in diameter. Collection of $^{12}C^-$, $^{13}C^-$ and $^{13}CH^-$ ions was simultaneous. Before analysis, targets of interest were pre-sputtered with Cs^+ ions to locally remove gold coating and possible surface contamination, and secondary ions were centered in the field aperture. To target micrometer to sub-micrometer size organic particles using the 1-µm spot condition, 10 µm x 10 µm $^{13}C^-$ ion images were generated prior to analysis (Supplementary Images), and the target area was positioned with repeated X-Y translations during continuous ion imaging, which allows sub-micrometric lateral accuracy in spite of the ~1-µm accuracy of the sample stage motors.

Carbon isotope ratios are shown in standard delta notation with respect to VPDB[1]. Correction for instrumental mass fractionation was achieved as follows. We bracketed each series of samples with unknown $\delta^{13}C$ with 8 (4+4) measures of $\delta^{13}C_{meas}$ on anthracite standards UWLA-1 and/or LGIS-A1 (Supplementary Tables 2-8) mounted together with unknown samples, hence allowing evaluations of electron multiplier (EM) aging and other machine drifts. The α bias correction factor is calculated using equation (1) from the $\delta^{13}C_{true}$ of these anthracites measured using bulk $\delta^{13}C_{org}$ analyses (Williford et al., 2016) and the uncorrected $\delta^{13}C_{meas}$ value measured with SIMS. The gain of the EM was monitored between analyses of anthracite standards and its drift, if any, was compensated by adjusting the high voltage setting (Williford et al., 2016).

$$\textbf{(1)} \qquad \boldsymbol{\alpha = (1000 + \delta^{13}C_{meas}) \div (1000 + \delta^{13}C_{true})}$$

The bias correction factor may vary with chemical compositions. Bias caused by differences in H/C ratios (or apparent H/C ratios measured as $^{13}CH^-/^{13}C^-$ ions) between unknown samples and standards may need correction (Sangély et al., 2005; Williford et al., 2016). This bias, α*, is derived from the determination of α on a series of carbonaceous matter standards (ambers, coals, anthracites, shungite), each displaying spatially homogeneous $^{13}CH^-/^{13}C^-$ ratios and $\delta^{13}C$ values, and selected to cover the broadest possible range of $^{13}CH^-/^{13}C^-$ ratios (Williford et al., 2016). Their $\delta^{13}C_{org}$ compositions were measured in bulk (Williford et al., 2016 and Supplementary Table 2). The α* value of each of these standards is derived from its α value divided by the α of the bracketing standard UWLA-1, hence correcting for the machine instrumental fractionation caused by physical properties other than the difference in structure and composition of the carbonaceous standards. For each instrumental session, α* of the carbonaceous standards plotted linearly with $R^H_{meas} = {}^{13}CH^-/^{13}C^-$

(Supplementary Tables 3-8). Therefore, the linear relationship was used to derive a general expression of α* that can be used to correct instrumental mass fractionation linked with varying apparent H/C of unknown samples as defined in equation (2), with $\alpha^* = -0.043491 \times R^H + 1.002305$ ($R^2 = 0.93$) for 6-µm spot analyses, $\alpha^* = -0.037833 \times R^H + 1.002324$ ($R^2 = 0.90$) for 3-µm spot analyses, and $\alpha^* = -0.069964 \times R^H + 1.003831$ ($R^2 = 0.90$) for 1-µm spot analyses (Supplementary Tables 4, 6, and 8).

$$\textbf{(2)} \qquad \boldsymbol{\alpha^* = \frac{\alpha_{std}}{\alpha_{UWLA-1}} = a \times R^H_{meas} + b}$$

However, we note that this correction was determined for each session using settings that may be specific to these analyses and WiscSIMS Lab. These α* values should not be applied to other measurements without analytical verification. Altogether, the organic carbon isotope ratio of unknown samples is derived from equation (3), where α is the value measured on bracketing anthracite standards and α* is derived from equation (2) using the R^H ratio measured on the unknown sample together with $\delta^{13}C_{meas}$. In addition, an additional correction factor α' was needed to apply a cross-calibration between the standards UWLA-1 and LGIS-A1. α' is equal to 1 when the bracketing standard is UWLA-1, and to the α* of LGIS-A1 when LGIS-A1 is the bracketing standard.

$$\textbf{(3)} \qquad \boldsymbol{\delta^{13}C_{org} = \frac{\delta^{13}C_{meas}+1000}{\alpha \times \alpha^* \times \alpha'} - 1000}$$

Bias is defined as the mean α of the bracketing standard analyses, and external precision is defined as two standard deviations (2SD) of these bracketing analyses. Internal precision is defined as two standard errors (2SE) of the multiple measurements (cycles) of each analysis. Williford et al. (2016) have shown that the accuracy of SIMS data recorded at low $^{12}C^-$ count rate in mixed phases can be significantly degraded. Additional bias arising from the presence of chlorite and/or calcite in the analyzed volume are evaluated below together with their effect on internal precision. Both 2SD and 2SE are reported in Supplementary Tables 3-10. The total range of 2SD is 0.08–1.33‰, whereas 2SE values display a larger range of 0.44–8‰ reflecting data recorded at lower count rates. The filtering of data with low count rates relative to that of pure OM standard restrains the range of 2SE to 0.44–1.6. For data filtered as detailed below the mean of 2SD values—weighed by the number of filtered analyses for each bracket—is 0.72, smaller than the mean of 2SE of 0.99. Accordingly, we report 2SE values as error bars in figures 8-11. Only for the data of figure 4 we report errors as the larger 2SD values instead of 2SE. Finally, statistical analyses of SIMS data (Kernel density plots, Welsh two sample t-test, Mann-Whitney U test) were conducted using the software *R* version 3.4.2.

3.5. Bulk-rock elemental analyses

Bulk rock elemental analyses of Fe, Mn and As were performed after fusion in $LiBO_2$ and dissolution in a HNO_3-H_2O_2-glycerol mixture (at CRPG-SARM) as detailed in Carignan et al. (2001). All Fe has been converted to Fe_2O_3 and is thus reported in wt.% Fe_2O_3. Similarly, Mn is reported as wt.% MnO. As is reported in ppm. Fe and Mn were measured by inductively coupled plasma optical emission spectrometry, whereas As was measured by inductively coupled mass spectrometry (Carignan et al., 2001). Detection limits on blanks were 0.04 wt.% for Fe_2O_3, 0.001 wt.% for MnO, and 1.6 ppm for As. The uncertainties measured on geochemical reference materials (Carignan et al., 2001) were <2% (Fe_2O_3), <5% (MnO) and <15% (As).

4. Results

Petrographic observations and variations in organic S/C distinguish three types of organic matter in the two studied stromatolites. Organic carbon isotope microanalyses are grouped by OM type in Supplementary Tables 9 and 10. The Supplementary Images file displays the precise localization of each SIMS analysis target.

4.1. Petrography of the stromatolites

Stromatolite samples KGI68.2 and 69.2a comprise the same three main mineral assemblages (Fig. 3 and Lepot et al. 2008, 2009a). First, the light-coloured layers are predominantly composed of micritic to microsparritic calcite, with minor quartz, chlorite, muscovite, pyrite and anatase. Second, the black mud-type layers are poor in calcite but rich in quartz, chlorite, muscovite, and also display variable amounts of pyrite and anatase. Third, clastic grains are interspersed and sometimes dominate in calcite-rich layers (Fig. 3C). These clastic grains are often similar in composition (chloritic and/or Ti-rich) and shape to the volcanoclastic material of the Mingah Member (Lepot et al., 2011). Calcite pseudomorphs after cubic halite crystals occur embedded in stromatolitic layers of both samples (e.g. Fig. 3B), some displaying diagnostic hopper growth structures (Philippot et al., 2009).

Two main types (A and B) of OM have previously been identified in these samples (Lepot et al., 2009a), and an additional type (C) is described below. Type-A OM is distributed in seams and clusters at the grain boundaries of quartz and/or finely layered chlorite. Seams of Type-A OM occur only in mud-type layers and are variably interspersed with chlorite and pyrite (Fig. 3E). Chloritic clusters of Type-A OM occur both in mud-type layer and carbonate-dominated layers (Fig. 3D-E). Type-B OM comprises clusters of sub-rounded globules smaller than 2 µm in diameter embedded in calcite crystals of carbonate-dominated layers (Fig. 3D). Chloritic clusters of intergranular Type-A OM are sometimes found at the center of clusters of Type-B globules in calcite—the largest example of this distribution is shown in Fig. 3D. Type-C OM consists of an elongated ca. 50x80-µm nodule that is mostly composed of OM. This nodule is surrounded by quartz, calcite, chlorite and muscovite (Fig. 4) and cut across by chlorite+muscovite veinlets, and interspersed with pyrite, chalcopyrite, chlorite, muscovite, quartz and U-rich microcrystals. A large hole (Fig. 4A) has a size and central disposition reminding of that of U-rich crystals commonly found in bitumen nodules (Rasmussen, 2005; Williford et al., 2016). Such a crystal might have been dissolved or torn away during polishing. This nodule is located in a layer rich in volcanoclastic material of sample 69.2a. Two similarly-shaped nodules with diffuse OM and abundant pyrite, chlorite and muscovite occur in another layer rich in (volcano)clastic material of the same sample (fig. 7 of Lepot et al., 2009a).

Semi-quantification of organic sulfur using SEM-EDXS of sulfide-free zones indicated that Type-A and -C OMs are poor in organic S (S/C proxy of 0.01–0.08, mean 0.04), whereas Type-B OM is variably enriched in organic S (S/C proxy of 0.01–0.38, mean 0.16), consistent with previous transmission electron microscopy (Lepot et al., 2009a). NanoSIMS analyses revealed atomic S/C of

0.003–0.004 in Type-A OM in a chlorite cluster and atomic S/C of 0.031–0.042 in Type-B OM in adjacent calcite (Fig. 5). The thiophenic nature of organic S suggested by C K-edge XANES (Lepot et al., 2009a) was confirmed with the S L-edge XANES spectrum of Type-B organic globules (Fig. 6). The latter display two main bands at 166.6 eV and 173.5 eV that correspond respectively to the 2p→σ*(C–S) transition and S3d orbitals of (poly)thiophenes (Tourillon et al., 1988; Riboulleau et al., 2000) and that are absent in S-bearing minerals (Fleet, 2005).

Finally, bulk-rock analyses of samples KGI68.2 and 69.2a yielded 3.64 and 3.92 wt.% Fe_2O_3, respectively, 0.30 and 0.37 wt.% MnO, respectively and 3.02 and 4.12 ppm As, respectively.

4.2. $\delta^{13}C$ of Type-A OM associated with quartz

Two distinct seams of Type-A OM, where the only mineral matrix is quartz, were analyzed multiple times to evaluate microscale homogeneity and matrix effects with SIMS using 3-µm spot size. The $\delta^{13}C_{org}$ values measured in Type-A OM associated with quartz range between -56.1 and -54.1 ‰ (n=7, mean -55 ‰) ± 2SE of 0.5 to 1.6 ‰ (mean ± 1 ‰). In each seam, all $\delta^{13}C_{org}$ values are similar within 2SE error (Fig. 7A-C) supporting intra-seam isotopic homogeneity. The $^{13}CH^-/^{13}C^-$ ratios of these OM seams range between 0.075–0.085, with the exception of one low count rate outlier with $^{13}CH^-/^{13}C^-$ ratio of 0.094 (Fig. 7C). Similar $\delta^{13}C_{org}$ values are found irrespective of the $^{13}CH^-/^{13}C^-$ ratios. Moreover, the quartz to OM concentration ratio in each SIMS spot is proportional to the ratio of the $^{12}C^-$ signal in the measured spot to the $^{12}C^-$ signal of a pure anthracite standard. Variable quartz concentrations do not appear to bias the $\delta^{13}C$ signal (Fig. 7D).

4.3. $\delta^{13}C$ of Type-A OM associated with chlorite

A wide range of $^{13}CH^-/^{13}C^-$ ratios between 0.078 and 0.158 was measured in chlorite-rich clusters of Type-A OM (Supplementary Table 9). Two chlorite-rich clusters were measured repeatedly with 3- and 1-µm spot sizes to sample zones with variable OM to chlorite (± minor quartz) concentration ratios (Figs. 8-9). In each cluster, the $\delta^{13}C_{org}$ values were negatively correlated with $^{13}CH^-/^{13}C^-$ ratios (Fig. 8D, 9A). In a cluster (*q5chip1* in Fig. 8), a 4.6 ‰ (± 0.5–0.9 ‰ 2SE) decrease in $\delta^{13}C_{org}$ values was observed over a $^{13}CH^-/^{13}C^-$ ratio range of 0.079–0.103. In a second cluster (*c14* in Fig. 8), a 3.9 ‰ (± 0.5–0.9 ‰ 2SE) decrease in $\delta^{13}C_{org}$ values was observed over a $^{13}CH^-/^{13}C^-$ ratio range of 0.079–0.098. Bias imparted (to the $\delta^{13}C$ values) by variable apparent H/C ratios ($^{13}CH^-/^{13}C^-$) in OM can be calculated using the α* correction expressed in δ notation (see Supplementary Table 6, IMF $\delta = -37.833 \times {}^{13}CH^-/^{13}C^- + 2.3236$), leading to a bias <1 ‰ over the 0.079–0.103 range of $^{13}CH^-/^{13}C^-$ ratios. Hence, variable apparent H/C ratios in OM may not alone account for the observed range of $\delta^{13}C_{org}$ values (up to 4.6 ‰ variation) in these two chlorite clusters. Importantly, the $^{13}CH^-/^{13}C^-$ ratios were found to increase with increasing chlorite/OM concentration ratios (Fig. 8E). Therefore, a large bias occurs on the measurements of $\delta^{13}C_{org}$ and $^{13}CH^-/^{13}C^-$ ratios of OM in presence of chlorite. We interpret this bias as the result of the recombination of OM-derived C ions with H ions (Spool, 2004)

derived from chlorite (Deloule et al., 1991) in Supplementary Discussion 1, where we suggest implications for SIMS measurement of δD (Deloule and Robert, 1995).

We could not derive an accurate correction curve to correct this matrix bias in chlorite-rich domains using the present data because we could not determine the H content in chlorite and derive end-members to use simple mass balance equations. However, the $\delta^{13}C_{org}$ values recorded in chlorite-poor zones where $^{13}CH^-/^{13}C^-$ ratios lie in the same range as in the H-free quartz (<0.085) should be close to those of chlorite-free OM within 2SE error. Only some of the analyses in OM+chlorite zones performed with 1- and 3-µm spots satisfy this criterion. Chloritic zones in sample KGI68.2 and KGI68.2' that satisfy the filtering criterion $^{13}CH^-/^{13}C^- < 0.085$ display $\delta^{13}C_{org}$ values ranging between -55.4 and -50.6 ‰ (± 0.4 to 0.9 ‰ 2SE) and averaging at -52.5 ‰ (n = 11). In sample 69.2a, none of the SIMS measurements in chloritic zones satisfy this filtering criterion as all the targets had low OM/chlorite relative abundances.

The range of $\delta^{13}C_{org}$ in Type-A OM analyzed near quartz in the absence of chlorite is small and overlaps with the $\delta^{13}C_{org}$ values recorded with no/minimal interference of chlorite (at $^{13}CH^-/^{13}C^-$ <0.085; Supplementary Table 9). All Type-A OM filtered with $^{13}CH^-/^{13}C^-$<0.085 were recorded at $^{12}C_{meas}^-/^{12}C_{anthracite}^-$ >0.22, thus providing acceptable count rates (>0.1: Williford et al., 2016). After filtering out analytical spots in which chlorite was evidenced by coupled SEM-EDXS detection and increased $^{13}CH^-/^{13}C^-$>0.085, we expect that the $\delta^{13}C_{org}$ values recorded in the vicinity of chlorite are accurate within 2SE error. Henceforth, all Type-A OM (associated with quartz and/or chlorite) will be grouped, yielding a range of $\delta^{13}C_{org}$ between -56.1 to -50.6 ‰ ±0.4–1.6 ‰ (2SE), with a mean value of -53.5 ‰.

4.4. $\delta^{13}C$ of Type-B OM in carbonates

The Type-B globules of OM in carbonates are generally smaller than the SIMS sampling size. Although carbonates only yield 1.7 to 2.3 % of the $^{12}C^-$ count rate relative to the anthracite OM standard (Supplementary Table 10), the volume of sputtered carbonate may not be negligible compared to the volume of OM globules. The total $^{12}C^-$ count rates measured on OM globules in carbonates ($^{12}C_{meas}^-$, see equation 4, with $^{12}C_{carb}^-$ and $^{12}C_{org}^-$ the ion count rates from carbonates and OM, respectively) relative to that of pure anthracite ($^{12}C_{anthracite}^-$) were, using 6-µm spot: 4.4–12.2 % (mean 8.4 %, SD=2.7 %), using 3-µm spot: 12.7–29.6 % (mean 21 %, SD=5.2 %), and using 1-µm spot 3.8–35.2 % (mean 14.4 %, SD=10.1 %).

(4) $$^{12}\boldsymbol{C}_{\boldsymbol{meas}}^{-} = {}^{12}\boldsymbol{C}_{\boldsymbol{carb}}^{-} + {}^{12}\boldsymbol{C}_{\boldsymbol{org}}^{-}$$

An interference of C_{carb} is possible in the measurement of $\delta^{13}C_{meas}$ in micrometric organic globules because of the low OM volume and the large difference in $\delta^{13}C_{meas}$ between pure carbonate and organic-rich targets. However, knowing the relative fractions of carbonate C_{carb} and organic C_{org} and the uncorrected SIMS-measured $\delta^{13}C_{meas(pure\text{-}carb)}$ of pure carbonate spots (-36.8 ±14.5 ‰ 2SE, -34.2 ±5.9 ‰ and -40.7 ±7.2 ‰ with 6-, 3- and 1-µm spots respectively), can help estimate the $\delta^{13}C_{org}$ of micrometric globules using mass balance. Homogeneous bulk $\delta^{13}C_{carb}$ values of 0.4 and 0.9 ‰ were

recorded in bulk carbonate of KGI68.2 and 69.2a, respectively (Thomazo et al., 2009b). In addition, $\delta^{13}C_{carb}$ values of micro-drilled Tumbiana stromatolites display <1 ‰ variation (Slotznick and Fischer, 2016). Hence, we assume that the $\delta^{13}C_{meas(pure\text{-}carb)}$ value is constant in our samples for each SIMS analytical setup (i.e. at constant instrumental mass fractionation).

To make this mass-balance estimation, we define the fraction $\boldsymbol{f}$ of $^{12}C_{org}^-$ ions from OM in the total measured $^{12}C^-$ count rate ($^{12}C_{meas}^-$, see equation 4) using equation (5).

(5) $$^{12}\boldsymbol{C}_{\boldsymbol{org}}^{-}(\boldsymbol{f}) = \boldsymbol{f} \times {}^{12}\boldsymbol{C}_{\boldsymbol{meas}}^{-}$$

At any value of $\boldsymbol{f}$, the flux of $^{12}C^-$ ions generated by carbonates is defined using equation (6).

(6) $$^{12}\boldsymbol{C}_{\boldsymbol{carb}}^{-}(\boldsymbol{f}) = (\mathbf{1}-\boldsymbol{f}) \times {}^{12}\boldsymbol{C}_{\boldsymbol{meas}}^{-}$$

The known limit conditions to equations (5-6) are given in (7) and (8), and can be applied to yield equation (9).

(7) $^{12}\boldsymbol{C}_{\boldsymbol{meas}}^{-}(\boldsymbol{f}=\mathbf{1}) = {}^{12}\boldsymbol{C}_{\boldsymbol{anthracite}}^{-}$, i.e. the count rate measured on pure OM

(8) $^{12}\boldsymbol{C}_{\boldsymbol{meas}}^{-}(\boldsymbol{f}=\mathbf{0}) = {}^{12}\boldsymbol{C}_{\boldsymbol{pure-carb}}^{-}$, i.e. the count rate measured on pure (OM–free) carbonate

(9) $$^{12}\boldsymbol{C}_{\boldsymbol{carb}}^{-}(\boldsymbol{f}) = \frac{{}^{12}\boldsymbol{C}_{\boldsymbol{anthracite}}^{-} - {}^{12}\boldsymbol{C}_{\boldsymbol{org}}^{-}(\boldsymbol{f})}{{}^{12}\boldsymbol{C}_{\boldsymbol{anthracite}}^{-}} \times {}^{12}\boldsymbol{C}_{\boldsymbol{pure-carb}}^{-}$$

Altogether, $\boldsymbol{f}$ can be expressed in direct relationship with measured values using equation (10).

(10) $$\boldsymbol{f} = \left(\mathbf{1} - \frac{{}^{12}\boldsymbol{C}_{\boldsymbol{pure-carb}}^{-}}{{}^{12}\boldsymbol{C}_{\boldsymbol{meas}}^{-}}\right) \div \left(\mathbf{1} - \frac{{}^{12}\boldsymbol{C}_{\boldsymbol{pure-carb}}^{-}}{{}^{12}\boldsymbol{C}_{\boldsymbol{anthracite}}^{-}}\right)$$

A negative correlation is observed between $\delta^{13}C_{org}$ (eq. 3) and $\boldsymbol{f}$ values using both 1- and 6-µm spot analyses of Type-B globules in calcite (Fig. 10A). Therefore, although intrinsic heterogeneities may occur in the isotopic composition of organic globules, a mixture trend could be demonstrated between carbonate C_{carb} and organic C_{org} in the analyzed spots. Accordingly, the raw $\delta^{13}C_{meas(org+carb)}$ measured on mixed OM+carbonate can be used to derive the raw (not yet corrected from α and α* bias) isotopic composition of the organic fraction ($\delta^{13}C^*_{meas}$) in each spot, corrected from carbonate interference, using equation (11).

(11) $$\boldsymbol{\delta^{13}C}_{\boldsymbol{meas}}^{*} = \frac{\boldsymbol{\delta^{13}C}_{\boldsymbol{meas(org+carb)}}}{\boldsymbol{f}} + (\mathbf{1}-\boldsymbol{f}) \times \boldsymbol{\delta^{13}C}_{\boldsymbol{meas(pure-carb)}}$$

In turn, the obtained $\delta^{13}C^*_{meas}$ value has to be corrected from α and α* bias (and cross-calibrated with α', see above). However, α* derives from $R^H_{meas} = {}^{13}CH^-/{}^{13}C^-$, which is expected to decrease in presence of H-free carbonate. Accordingly, the R^H of organic matter (R^H_{org}) is corrected by subtracting the carbonate interference (non-zero R^H_{carb}) to R^H_{meas} using equation 13 (following eq. 12).

(12) $$\boldsymbol{R}_{\boldsymbol{meas}}^{\boldsymbol{H}} = \boldsymbol{f} \times \boldsymbol{R}_{\boldsymbol{org}}^{\boldsymbol{H}} + (\mathbf{1}-\boldsymbol{f}) \times \boldsymbol{R}_{\boldsymbol{carb}}^{\boldsymbol{H}}$$

(13) $$\boldsymbol{R}_{\boldsymbol{org}}^{\boldsymbol{H}} = \frac{\boldsymbol{R}_{\boldsymbol{meas}}^{\boldsymbol{H}}}{\boldsymbol{f}} + \left(\mathbf{1} - \frac{\mathbf{1}}{\boldsymbol{f}}\right) \times \boldsymbol{R}_{\boldsymbol{carb}}^{\boldsymbol{H}}$$

The correction factor α_2* can then be calculated from equation (2) using R^H_{org} derived from equation (13) instead of R^H_{meas}. Finally, the isotopic composition of organic globules corrected from carbonate interference, apparent H/C bias and matrix effects can be reported against VPDB as $\delta^{13}C^*_{org}$ according to equation (14).

(14) $$\boldsymbol{\delta^{13}C^*_{org} = \frac{\delta^{13}C^*_{meas}+1000}{\alpha \times \alpha_2{}^* \times \alpha'} - 1000}$$

The measurements of $\delta^{13}C_{meas(pure\text{-}carb)}$ we used to derive $\delta^{13}C^*_{org}$ values have low counting statistics (±5–7 ‰ 2SE using 1- and 3-µm spots, ±14–15 ‰ using 6-µm spot). This uncertainty must be propagated to the estimation of the 2SE of $\delta^{13}C^*_{org}$ using equation (15).

(15) Composite error: $$\mathbf{2SE^*(\delta^{13}C^*_{org}) = \frac{2SE(\delta^{13}C_{meas})}{f} + (1-f) \times 2SE(\delta^{13}C_{meas(pure-carb)})}$$

Unfiltered $\delta^{13}C^*_{org}$ values (Fig. 10B) range between -75.8 and -48.1 ‰ (mean -59.3 ‰) with a poor precision of ±1.3–12 ‰ 2SE* (mean 2.5 ‰). All Type-B OM spots with f>0.9 were recorded with count rate ratios $^{12}C_{meas}{}^-/^{12}C_{anthracite}{}^-$ >0.15, which are high enough (>0.1) to allow accurate measurements (Williford et al., 2016). The accuracy of the correction yielding $\delta^{13}C^*_{org}$ values is estimated by 2SE* (eq. 15). At f>0.9, 2SE* becomes acceptable (<2.2 ‰). Using the data filtering criterion of f>0.9, which applies only to OM in carbonates and that is equivalent to 2SE*<2.2 ‰, (see eq. 15), $\delta^{13}C^*_{org}$ values recorded in Type-B globules range between -65.2 and -52.5 ‰ (mean -58.8 ‰) ± 1.3–2.2 ‰ 2SE*. These $\delta^{13}C^*_{org}$ values filtered with f>0.9 correspond to a range of $\delta^{13}C_{org}$ values (uncorrected from carbonate interference) of -61.5 to -49.1 (mean -55.6 ‰) ± 1–1.5 ‰ 2SE. We note that $\delta^{13}C^*_{org}$ values filtered with the criterion f>0.7 show a similar range (-65.2 to -52.5 ‰). At f>0.7, the mean $\delta^{13}C^*_{org}$ is -58.2 ‰ for 1- and 3-µm spots with 2SE* of 1–3.5 ‰ and -57.9 ‰ (with 2SE* increasing up to 6 ‰) when including 6-µm spots, hence similar to the mean with f>0.9 (Fig. 10B). This indicates that the lower precision of the $\delta^{13}C_{meas(pure\text{-}carb)}$ measurement influences little the correction of equation 14 when f is sufficiently high (>0.7). In contrast, at f<*0.7* $\delta^{13}C^*_{org}$ values deviate significantly.

4.5. $\delta^{13}C$ of Type-C OM

In the nodule of Type-C OM of sample 69.2a, targets were large enough to avoid chlorites, as confirmed with SEM-EDXS mapping (Fig. 4). In this nodule, the $^{13}CH^-/^{13}C^-$ ratios range between 0.079 and 0.089 (mean 0.083) and values were not correlated with $\delta^{13}C$, consistent with measurements unbiased by chloritic H. The $\delta^{13}C_{org}$ values range between -48.0 and -39.1 ‰ (± 1.33 ‰ 2SD) and average at -44.2 ‰ (n = 10, SD ±2.6 ‰). The spatial distribution of $\delta^{13}C_{org}$ values is zoned with the lower values in the lower left and upper right extremities of the nodule, and with higher values in the central part.

4.6. Data assessment and summary

Evaluation of bias correction methods and data filtering criteria is required to address the significance of the isotopic heterogeneities described.

The correction of the bias on $\delta^{13}C_{org}$ values induced by variable apparent H/C contents in OM (Sangély et al., 2005; Williford et al., 2016) yielded a range of correction factors (expressed as 1000.log(α*)) of -0.92 ‰ to 0.27 ‰ (mean -0.3 ‰) in the measured range of $^{13}CH^-/^{13}C^-$ ratios (excluding chloritic regions with $^{13}CH^-/^{13}C^->0.085$). This narrow range cannot explain the observed isotopic heterogeneities.

The values of $\delta^{13}C^*_{org}$ and $\delta^{13}C_{org}$ do not correlate to variations in S/C ratios (R^2=0.2 for a linear fit of all data in Fig. 11, R^2=0.01 for a linear fit of $\delta^{13}C^*_{org}$ in Type-B globules only *versus* S/C proxy). This observation is consistent with the observation that SIMS measurements of S isotope ratios in OM are not correlated with S/C (Bontognali et al., 2012). In S-rich kerogens and in kerogen residues after thermal decomposition, S–C bonds are generally at least an order of magnitude less abundant than H–C bonds (Riboulleau et al., 2000). Kerogen of the Tumbiana stromatolites display bulk atomic H/C of ~0.3 (Strauss and Moore, 1992) whereas the atomic S/C in S-rich globules only reached ~0.042 (Fig. 5). In turn, assuming that the isotopic fractionation associated with S–C bond breakup has the same magnitude as that associated with H–C breakup (<5 ‰, Supplementary Tables 4, 6 and 8), the former would be smaller than our 2SE* analytical precision of ca. 1.3–2.2 ‰.

Statistical analyses of the C isotope data, filtered according to above criteria (***f***>0.9, $^{13}CH^-/^{13}C^-$ <0.085), is shown in Supplementary Table 11. The Wilcoxon-Mann-Whitney test indicates that the filtered but uncorrected $\delta^{13}C_{org}$ values recorded in Type-B globules are significantly (p=2.5 %) lower (mean -55.6 ‰, -61.5 to -49.1 ‰ ±1–1.6 ‰ 2SE, Supplementary Table 10) than $\delta^{13}C_{org}$ values recorded in Type-A OM (mean -53.5 ‰ ±1.8 ‰ SD, -56.1 to -50.6 ‰ ±0.4–1.6 ‰ 2SE). Although their mean values are close within error, uncorrected Type-B OM displayed a group of $\delta^{13}C_{org}$ values that are significantly lower within error (down to -61.5 ‰). More importantly, corrected ($\delta^{13}C^*_{org}$) values of Type-B OM (-65.2 to -52.5 ‰ ± 1.3–2.2 ‰ 2SE*, mean -58.8 ‰ ±3.6 ‰ SD) are significantly lower than $\delta^{13}C_{org}$ values of Type-A OM, passing the Wilcoxon-Mann-Whitney test with p=0.0022 %. Finally, the $\delta^{13}C_{org}$ values of Type-C OM occurring only in sample 69.2a (-48.0 to -39.1 ‰ ± 1.3 ‰ 2SD) do not overlap with the values recorded in all Type-A and -B OM.

5. Discussion

5.1. OM migration

Large pyrobitumen nodules associated with radioactive grains are common in the Fortescue Group, including in ~2.75 Ga old fluviolacustrine deposits of the Hardey Formation (Buick et al., 1998; Thorne and Trendall, 2001; Rasmussen et al., 2009) and 2.63 Ga old shales of the Jeerinah Formation (Rasmussen, 2005). The presence of U-rich grains, of chalcopyrite and the zonation in $\delta^{13}C_{org}$ values observed in the nodular Type-C OM (Fig. 4) are also consistent with formation as pyrobitumen (Rasmussen, 2005; Sangély et al., 2007). The $\delta^{13}C_{org}$ zonation could be the product of abiotic synthesis of the pyrobitumen through catalytic hydrogenation of CO_2 or radiolytic alteration of

biomass-sourced oil that segregated onto U-minerals (Sangély et al., 2007). The apparent absence of link between H/C ratio and $\delta^{13}C_{org}$ values in the nodule (Supplementary Table 9) favors the biogenic interpretation (Sangély et al., 2007).

This pyrobitumen nodule features $\delta^{13}C_{org}$ values that are 3–12 ‰ higher than those determined from both Type-A and Type-B OM. Similarly, U-associated pyrobitumen nodules in the ~2.5 Ga Mount McRae Shale feature 2–8 ‰ ^{13}C-enrichments compared to co-occurring kerogen (Williford et al., 2016). The 3–12 ‰ ^{13}C-enrichment in Type-C compared to Type-A OM may be explained by a combination of isotope fractionations associated with bitumen mobilization (up to +3.8 ‰: Des Marais, 2001; Close et al., 2011) and radiolysis (up to about +8 ‰: Leventhal & Threlkeld, 1978; Sangély et al., 2007).

Alternatively, Type-C OM may have migrated through the Tumbiana Formation from an exogenous source. It has been shown that the most ^{13}C-depleted kerogens of the Fortescue Group occur in association with shallow lakes with mafic catchments, such as the studied stromatolites (Eigenbrode and Freeman, 2006; Flannery et al., 2016; Stüeken et al., 2017). In contrast, lakes with felsic catchments and open sea deposits typically display higher $\delta^{13}C_{org}$ values between -50 and -20 ‰ (Eigenbrode and Freeman, 2006; Flannery et al., 2016; Stüeken et al., 2017). Moreover, the siltstones of the Tumbiana Formation at the studied locality display $\delta^{13}C_{org}$ values between -44.9 and -23.8 ‰, except for sample GIS88.8 (Thomazo et al., 2009b) that we latter re-evaluated as an interbedded carbonate/mudstone (not shown). By analogy with the Phanerozoic, these siltstones including the millimetric siltstone layer hosting the nodule of Type-C OM (Fig. 3C) were likely more prone to Archean oil sequestration than the mudstones and possibly (depending on porosity) than the stromatolites of the Tumbiana Formation. The grains in the volcanoclastic siltstones interbedded within the mudstones/carbonates deposits of the Meentheena Member and the underlying Mingah Member are coated with organic films (Lepot et al., 2011). In addition, OM was also found in vesicles of the overlying Maddina basalts at the studied locality (Lepot et al., 2009b). Together, these observations suggest that, similar to Type-C pyrobitumen, OM with $\delta^{13}C_{org}$ values exceeding -48 ‰ may have migrated from elsewhere, originating from marine or felsic-housed lacustrine systems. Alternatively, the OM in the siltstones, particularly that within the Mingah Member may have originated from the primary biomass that decomposed into CO_2 and/or CH_4 (Thomazo et al., 2009b). These carbon compounds could have been reprocessed by either Acetyl-CoA-dependent metabolisms and/or methanotrophs. The respective importance of each of these metabolism is discussed below.

5.2. Acetyl-CoA pathways

The acetyl-CoA pathway can form acetate autotrophically using H_2 (Fig. 1C), and imparts ^{13}C-depletions of -50 to -60 ‰ to the acetate relative to parent CO_2 and of -12.9 to -20.6 ‰ to the biomass relative to parent CO_2 (Gelwicks et al., 1989; Preuß et al., 1989; Blaser et al., 2013; Freude and Blaser, 2016). This ^{13}C-depleted acetate could, in principle, have been used by heterotrophs, transferring its ^{13}C-depleted signature to the sedimentary OM reservoir (Slotznick and Fischer, 2016). Indeed, the

ratio of acetate to biomass carbon produced by hydrogenotrophic acetogenesis is more than nine to one (Balch et al., 1977; Gelwicks et al., 1989; Freude and Blaser, 2016). Thus, assuming the only autotrophic producers were acetogens, 90% of the organic matter available for heterotrophs would have been ^{13}C-depleted acetate. The H_2 demand of acetogenesis may be fueled by fermentation of biomass (Fig. 1B), hydrothermal activity associated with ultramafic rocks (Mével, 2003; McCollom and Seewald, 2013; Konn et al., 2015), or possibly via atmospheric H_2 supply (Tian, 2005; Catling, 2006).

Ultramafic lavas could possibly have produced H_2 abiotically via low temperature serpentinization (Konn et al., 2015). Ultramafic (komatiitic) lavas, however, are only found in the Pyradie Formation (Thorne and Trendall, 2001). In contrast, other lavas of the Fortescue Group, including the Kylena Formation subaerial lavas underlying the Tumbiana Formation, are generally of basaltic-andesitic composition resulting from crustal contamination of an initially komatiitic magma (Thorne and Trendall, 2001; Mole et al., 2018). Consequently, the igneous rocks in proximity to the deposition center were not prone to serpentinization. Local metasomatism of basaltic flow tops occurred only after regional metamorphism of the Fortescue Group (White et al., 2014). In the absence of a vein system similar to that observed in Paleoarchean rocks (Ueno et al., 2004), and in the absence of distinct hydrothermally-derived Fe/S mineralization (Buick, 1992), no fluid conduits that could have delivered H_2-rich fluids to the Tumbiana lake system are recognized/identified.

Hydrogenotrophic microbial reduction of sulfate (Fig. 1D; Londry and Des Marais, 2003) and of Fe^{3+}-minerals (Fig. 1E; Etique et al., 2016) outcompete acetogenesis for H_2 (Hoehler et al., 1998, and fig. 3.9 in Madigan et al., 2009) just like sulfate- and iron-reducing bacteria outcompete methanogens for OM (Fig. 1G-I; Konhauser, 2007). The sulfur isotope systematics of the Tumbiana stromatolites display evidence for microbial sulfate reduction (Marin-Carbonne et al., 2018). In addition, the Fe-isotope signatures of some mudstones from the Tumbiana Formation require microbial Fe-reduction (Yoshiya et al., 2012). Furthermore, microbial reduction of arsenate with H_2 (Chung et al., 2006) may also have occurred as suggested by As-enrichments in specific laminae of the Tumbiana stromatolites (Sforna et al., 2014). Methanogenesis also outcompetes acetogenesis for H_2, except in special conditions such as low temperatures and/or low pH (Drake et al., 2006; Heuer et al., 2010). Nitrogen isotope ratios rather suggest that the Tumbiana lakes were alkaline (Stüeken et al., 2015b). Thus, microbial sulfate reducers, methanogens, and Fe-reducing bacteria, likely consumed a large fraction of the available H_2, limiting the potential to form ^{13}C-depleted acetate. Interestingly, a Tumbiana mudstone displayed two closely associated types of kerogen, with $\delta^{13}C_{org}$ of -52 ‰ and -34 ‰ that were interpreted as OM from the biomasses of methanotrophs and primary producers, respectively (Williford et al., 2016). Although the lower $\delta^{13}C_{org}$ values of -52 ‰ may have formed through assimilation of hydrogenotrophic acetate, the $\delta^{13}C_{org}$ values of -34 ‰ recorded by the co-existent kerogen is too low to reconcile with the biomass of acetogens alone (Preuß et al., 1989; House et al., 2003). Rather, this later value is best interpreted as the product of other primary producers such as photosynthesizers (House et al., 2000; Kaufman and Xiao, 2003; Williford et al., 2013) or hydrogenotrophic MSR using the acetyl Co-A pathway (Preuß et al., 1989). Moreover, Type-A and -B OM are both sulfurized and commonly associated with swarms of nano-pyrites (Fig. 5; Lepot et

al., 2009a; Marin-Carbonne et al., 2018). This observation of a strong coupling between sulfur cycling and OM is at odds with the inferred situation whereby production of hydrogenotrophic acetate required a termination of the more competitive MSR.

Alternatively, using analogy to modern settings, hydrogenotrophic acetogenesis can be fueled by the H_2 and CO_2 products of fermentation (Fig. 1B) of primary biomass with ^{13}C-depleted CO_2. However, in this case, the isotopic fractionation of hydrogenotrophic acetogenesis will be dampened in bulk and at the microscopic scale of kerogen formation by that of acetate and other molecules produced by fermentation metabolisms (Heuer et al., 2009; Heuer et al., 2010; Conrad et al., 2014), as well as by abiotic condensation of labile molecules (Vandenbroucke and Largeau, 2007) inherited from the primary biomass. In this case, the kerogen would likely not depart by more than ±10 ‰ from the composition of the primary biomass ($\delta^{13}C \geq$ -39.3 ‰, Figs. 1A, 1C-F), as developed in Supplementary Discussion 2. Importantly, to our knowledge, the formation of biomass with $\delta^{13}C_{org}$ values lower than -50 ‰ through the consumption of hydrogenotrophic acetate has never been observed directly, for example with the SIMS techniques coupled to fluorescence *in situ* hybridization used to reveal the isotopic composition of methanotrophic biomass (Orphan et al., 2001).

Thus it appears difficult to attribute bulk OM $\delta^{13}C_{org}$ values lower than -50 ‰ as well as microscale $\delta^{13}C_{org}$ as low as -65.2‰ in Type-B OM to heterotrophic consumption of acetate that was generated through fermentation and/or using fermentative H_2. In contrast, methanotrophic cells have been directly observed to carry the signature of parent methane as they displayed $\delta^{13}C_{cell}$ values usually much lower than -50 ‰ and even as low as -96 ‰ (Orphan et al., 2001; Orphan et al., 2002). The fact that ^{13}C-depletions imparted by production (Fig. 1F, 1I) and consumption (Figs. 1J-K) of methane can be, once cumulated, much larger than those imparted by hydrogenotrophic acetogenesis alone (Fig. 1C), favors the production of biomass with the most extreme ^{13}C depletions. For instance, the biomass of methane seeps can be dominated by methanotrophic consortia and display bulk $\delta^{13}C_{org}$ values as low as -72.2 ‰ (Michaelis et al., 2002). Extreme $\delta^{13}C_{org}$ values such as those associated with Type-B OM, going down to -65.2 ‰—and likely about 2 ‰ lower before thermal alteration (Hayes et al., 1983)—are thus best interpreted as the signature of methanotrophy in agreement with traditional inferences (Hayes, 1994; Hinrichs, 2002).

5.3. Record of methanotrophy in carbonates?

Oxidation of methane can occur aerobically (Hanson and Hanson, 1996), or anaerobically (AOM) using SO_4^{2-} (Knittel and Boetius, 2009), Fe^{3+}-oxides and Mn^{4+}-oxides (Beal et al., 2009; Norði et al., 2013; Sivan et al., 2014), and NO_3^- or NO_2^- (Raghoebarsing et al., 2006; Haroon et al., 2013). While aerobic methanotrophy promotes calcite dissolution (Krause et al., 2014), AOM promotes calcite precipitation (e.g., Michaelis et al., 2002) and may have contributed to the formation of the Tumbiana carbonates. Slotznick and Fisher (2016), however, argued that the texture and isotopic composition of carbonates in the Tumbiana Formation were incompatible with methanotrophy. On the basis of geochemical modelling they argued that $\delta^{13}C$ values of carbonates produced by AOM in Archean

environments should range between -2 and -30 ‰ (Slotznick and Fischer, 2016). Thus, the range of $\delta^{13}C_{carbonates}$ values (-0.9 to 1.2 ‰) reported by Slotznick and Fisher (2016) appeared too high to support AOM. Other studies, however, have reported a wider range of $\delta^{13}C_{carbonates}$ values (-10.9 to +1.9 ‰) that are more consistent with a methanotrophic origin (Eigenbrode and Freeman, 2006; Thomazo et al., 2009b; Coffey et al., 2013; Williford et al., 2016; Stüeken et al., 2017).

Importantly, the model of Slotznick and Fischer (2016) neglects to account for other generations of carbonates not related to AOM whose higher $\delta^{13}C$ values would mute the AOM-derived $\delta^{13}C$ signal (Flannery et al., 2016; Stüeken et al., 2017). The consortia responsible for AOM may thrive as endolithic communities in the pore-spaces of older, low-permeability seafloor carbonates (Marlow et al., 2014). Although, in the latter case, the seafloor carbonates likely formed through methanotrophy in the past (Greinert et al., 2002), such endolithic AOM may similarly thrive in shallow water stromatolites. Consistent with this view, sulfate-dependent AOM is suggested by $\delta^{13}C_{org}$ values ranging between -55.4 and -43.3 ‰ and $\delta^{34}S_{pyrite}$ ranging between -8.5 and +19 ‰ in millimeter-scale synsedimentary cavities of fluviolacustrine stromatolites of the 2.75 Ga Hardey Formation (Fortescue Group, Australia) (Rasmussen et al., 2009). A large fraction of stromatolitic carbonates could have been produced by photosynthesis, as suggested by stromatolitic textures including tufts (Flannery and Walter, 2012), clumps (Sim et al., 2012), and palisades (Buick, 1992). Photosynthesis associated with respiration can produce stromatolitic carbonates with $\delta^{13}C$ values of up to +4 ‰ (Andres et al., 2006). In addition, fixation of methanogenic CO_2 by phototrophs can produce stromatolitic carbonates with strongly positive (up to +16 ‰) $\delta^{13}C$ values (Birgel et al., 2015). Altogether, the $\delta^{13}C_{carbonate}$ signature of methanotrophy may have been diluted by other metabolic reactions active during the deposition of the Tumbiana Formation. We turn to SIMS analyses of $\delta^{13}C_{org}$ coupled to petrography to further address the metabolic signatures in the Tumbiana stromatolites.

5.4. Methanotrophy as a source of ^{13}C-depleted OM

The Precambrian kerogen sample with the lowest bulk $\delta^{13}C_{org}$ values (-60.9 ‰) originates from the Tumbiana Formation (Strauss et al., 1992). Here we report $\delta^{13}C^{*}_{org}$ values down to -65.2 ‰ associated with Type-B OM, which currently represent the lowest $\delta^{13}C_{org}$ values known in ancient, deeply-buried OM (Eigenbrode and Freeman, 2006; Thomazo et al., 2009a; Flannery et al., 2016). As discussed above, such extremely low $\delta^{13}C_{org}$ values may hypothetically originate from hydrogenotrophic acetogenesis, but are more commonly reconciled with methanotrophy.

The $\delta^{13}C_{org}$ values in our samples are dependent on OM type, with Type-A OM being enriched in ^{13}C compared to Type-B OM. A variety of interpretations can explain these isotopic differences. For example, aceticlastic, hydrogenotrophic, and methylotrophic pathways can generate CH_4 with distinct $\delta^{13}C$ values (Fig. 1F, 1I; Stüeken et al., 2017). Similarly, differences in pathways for aceticlastic methanogenesis by *Methanosaeta* and *Methanosarcina* genera may also explain such heterogeneities (Fig. 1I), although *Methanosarcina* may not have evolved until the late-Permian (Rothman et al., 2014). Differences in methanogenic pathways have been invoked to explain environmentally-

dependent (ocean *versus* alkaline lakes) variations in bulk-rock $\delta^{13}C_{org}$ values (Stüeken et al., 2017). In addition, variations in methane flux may also have impacted the isotopic fractionation of AOM communities (Hinrichs et al., 2000). While variable sources/flux of methane are viable at the bulk-sediment scale, they are more difficult to reconcile with the sub-millimeter-scale heterogeneities identified here (Figs. 3, 5) and would require that Type-A and Type-B OM formed at different times. The only type of OM found in mud-type laminae was Type-A, whereas in calcitic laminae Type-A OM was only found within clusters of Type-B OM (Fig. 3). This intimate association of Type-A and Type-B OM suggests they have been co-genetic.

Excluding variations in methane sources, the higher $\delta^{13}C_{org}$ values in Type-A OM may reflect aerobic methanotrophy, while the lower $\delta^{13}C_{org}$ values of Type-B OM could relate to AOM. Biomass from aerobic methanotrophs may display smaller ^{12}C-enrichment than that of their anaerobic counterparts (Fig. 1J-K; Orphan et al., 2002; Templeton et al., 2006). Stromatolite textures (Buick, 1992; Flannery and Walter, 2012; Sim et al., 2012) and Mo isotope ratios are consistent with production of O_2 within the Tumbiana Lake system (Stüeken et al., 2017). Contrastingly, Fe-isotope ratios indicate only partial oxidation of iron in an oxygen-limited environment (Nishizawa et al., 2010; Yoshiya et al., 2012). Aqueous Fe^{2+} was most likely produced by alteration of basaltic volcanic ash (Stüeken et al., 2017) that occurs throughout the stromatolites (Lepot et al., 2009a; Flannery et al., 2016) and in the thick underlying Mingah tuffs (Lepot et al., 2011). This Fe^{2+} could have served as a buffer, limiting oxygen availability in the sediment and potentially even in the water column, in turn limiting the role of aerobic methanotrophy in forming the observed $\delta^{13}C_{org}$ heterogeneities.

5.5. Sulfate-dependent methanotrophy

In the sulfate-permeated region of recent seafloor sediments, nearly all the methane flux is used up by AOM (Knittel and Boetius, 2009). Sulfate, possibly of atmospheric origin (Farquhar et al., 2000), was reduced by microorganisms in the Tumbiana Lake water and/or sediments (Marin-Carbonne et al., 2018). A significant fraction of this MSR could have proceeded through sulfate-dependent AOM pathways (Hinrichs, 2002). Unlike Type-A and Type-C OM, Type-B OM commonly displays enrichments in organic sulfur (Figs. 5, 11; Lepot et al., 2009a). Organic sulfur typically forms through polymerization of reduced sulfur species, including polysulfides (HS_x^-, S_x^{2-}), HS^-, and/or elemental sulfur (Werne et al., 2004). In contemporary settings, these reduced species are provided by MSR (Werne et al., 2004). Heterotrophic MSR (Fig. 1G) is an important possible pathway for sulfurization (Werne et al., 2004), but it has recently been proposed that sulfate-dependent AOM (Fig. 1K, L) can also drive OM sulfurization (Quijada et al., 2016). Sulfate-dependent AOM can be conducted by syntrophic consortia of anaerobic methanotrophic (ANME) archaea and MSR (Fig. 1K; Boetius et al., 2000; Orphan et al., 2001). Sulfate-dependent AOM, however, can also be performed independently by ANME group 2 (ANME-2) archaea (Fig. 1L; Milucka et al., 2012). Here, the ANME-2 archaea oxidize CH_4 and reduce sulfate to elemental S (intracellular S_8 polysulfides). This elemental S can diffuse outside ANME-2 to react with HS^- and form polysulfides such as HS_2^- (Milucka et al., 2012). Associated bacteria, instead, are responsible for disproportionating the product

polysulfide HS_2^- into HS^- and sulfate (Milucka et al., 2012). Interestingly, the polysulfides such as HS_2^- produced by these specific ANME-2 archaea are highly potent toward OM sulfurization (Werne et al., 2004).

Furthermore, ANME-2 are known to produce larger ^{13}C-depletions in biomass relative to those produced by ANME-1 methanotrophs (Fig. 1K; Orphan et al., 2002; Treude et al., 2007). Accordingly, the high organic S content and extreme ^{13}C-depletion observed in Type-B OM support an origin tied to sulfate-dependent AOM, possibly carried out by polysulfide-producing ANME-2 (Fig. 1L). If the ANME-2 produced S° and HS_2^- independently, OM sulfurization could have proceeded without sulfate-reducing bacteria. In addition, intracellular polysulfides in ANME-2 could have been preserved in OM for several thousand years (e.g., Lepot et al., 2014). Later during diagenesis, polysulfides could have implanted large amounts of organic S locally in Type-B OM. In this scenario, the sulfurization of biomass other than that of ANME-2, such as that of S-disproportionating bacteria, may be limited.

The large isotopic heterogeneity observed in Type-B OM can be explained via the admixture of MSR or S-disproportionating microbial biomass that can also produce highly ^{13}C-depleted biomass by consuming the ^{13}C-depleted CO_2 liberated from methanotrophy (Fig. 1K, Hinrichs et al., 2000; Orphan et al., 2002). Similarly, the higher $\delta^{13}C_{org}$ values and lower organic S abundance in Type-A OM relative to Type-B OM can be explained by biomass of MSR and/or S-disproportionating bacteria. Alternatively, Type-A OM may also be the product of sulfate-dependent ANME-1 in consortia with MSR. Microscale investigation of modern sediments/biofilms have demonstrated that the biomass of ANME-1 is less ^{13}C-depleted than that of ANME-2 (Fig. 1K, Orphan et al., 2002; Treude et al., 2007). Their production of HS^-, rather than S_8 or HS_2^-, would presumably be less efficient at promoting OM sulfurization (Werne et al., 2004), resulting in S-poorer OM. Consistent with this, we note the small concentration of organic sulfur associated with Type-A OM (Figs. 5, 11). Moreover, in another stromatolite from 68.9 m core depth, OM corresponding to textural Type A (in seams with chlorite and quartz) was observed in association with nanopyrites bearing the S-isotope signature of MSR (Marin-Carbonne et al., 2018). Together these observations are consistent with the hypothesis that Type-A OM also had a genetic history linked to sulfur-dependent AOM.

5.6. Nitrate/nitrite-dependent AOM

Among the other environmentally relevant chemical species that may have fueled AOM are nitrate and nitrite (Raghoebarsing et al., 2006). Recent investigations indicate that $NO_{2/3}^-$-dependent methanotrophs are bacteria operating without partner archaea (Ettwig et al., 2008). Unfortunately, to our knowledge, the C-isotope fractionations of the biomass of $NO_{2/3}^-$-dependent methanotrophs has yet to be measured. The available isotope fractionations measured on methane did not allow to clearly distinguish the various forms of methanotrophy (Rasigraf et al., 2012). Nitrate availability within the Tumbiana system has been proposed based on the extreme $\delta^{15}N$ values it records (Thomazo et al., 2011). These extreme $\delta^{15}N$ values have, however, been alternatively explained via NH_3 volatilization

processes (Stüeken et al., 2015b). Moreover, the availability of nitrate and nitrite during the Archean may have been limited in oxygen-poor environments by their reduction through denitrification and anaerobic ammonium oxidation (Zerkle and Mikhail, 2017; Zerkle et al., 2017; Luo et al., 2018) and possibly though microbial oxidation of Fe^{2+} (Miot et al., 2009; Klueglein et al., 2014). Therefore, similar to O_2, N-oxyanions may not have been readily accessible for methanotrophs.

5.7. Fe-, Mn-, As-dependent AOM

Perhaps more relevant than methanotrophy using O_2 or $NO_{2/3}^-$ in an anoxic Archean setting are Fe-/Mn-dependent AOM metabolisms (Fig. 1K; Beal et al., 2009). Arsenate reduction (Sforna et al., 2014) may also have potentially fueled AOM, although to the best of our knowledge, As-dependent AOM has not been documented in recent settings, and even if it was proven to be viable, the low As concentrations (≤4.12 ppm) likely render it unimportant in our samples.

Genetic studies of methane seep sediments associated with active Fe- and Mn-coupled AOM demonstrated that ANME-1 genes were significantly more abundant than those of ANME-2 (Beal et al., 2009). Accordingly, Fe- and/or Mn-coupled AOM would be expected to produce less negative $\delta^{13}C_{org}$ values (Orphan et al., 2002; Treude et al., 2007), which could explain the higher $\delta^{13}C_{org}$ values of Type-A OM relative to Type-B OM. The studied stromatolites (KGI68.2 and 69.2a) display Mn concentrations of 0.30 and 0.37 wt.% MnO and Fe-concentrations of 3.64 and 3.92 wt.% Fe_2O_3, respectively, that is atomic Fe/Mn ratios of about 10. Although Fe is much more abundant, AOM requires two times less Mn than Fe per mole of CH_4 oxidized (Beal et al., 2009). Possibly more relevant than the relative Fe/Mn concentrations in distinguishing the possible importance of these AOM pathways was the initial availability of Fe^{3+} and/or Mn^{4+}. Although abiotic Mn^{2+} oxidation by O_2 is slow, aerobic microbial oxidation favors Mn^{2+} over Fe^{2+} (Konhauser, 2007). In contrast, anaerobic photosynthetic oxidation of Fe^{2+} is possible (Konhauser, 2007), whereas anoxygenic photosynthetic oxidation of Mn has yet to be discovered (Jones and Crowe, 2013).

Molybdenum isotope fractionations recorded in the Tumbiana Formation (Stüeken et al., 2017) could have been produced by adsorption of Mo onto Mn^{4+}-oxides, Fe^{3+}-(oxyhydr)oxides, and sequestration into sulfide minerals (Kendall et al., 2017). Furthermore, Mn was not detected with SEM EDXS in the mineral assemblage associated with Type-A OM (i.e. chlorite), and instead Mn is essentially found as a minor Mn^{2+} component included in calcite (Lepot et al., 2008; Lepot et al., 2009a). Thus far, we lack petrographic and isotopic evidence that oxidized Mn participated in AOM.

In contrast, Type-A OM is intimately associated with Fe-bearing phases. Type-A OM and siliceous layers that exclusively host Type-A OM are also enriched in pyrite compared to calcitic layers that include Type-B OM (Lepot et al., 2009a; Thomazo et al., 2009b; Nishizawa et al., 2010; Marin-Carbonne et al., 2018). Moreover, the intimate association of Fe- and Mg-rich chlorites with Type-A OM (Figs. 3, 5, 8) suggests that some of these Fe-silicates could have formed as authigenic rather than clastic minerals, as seen in modern stromatolites (Lepot et al., 2009a; Burne et al., 2014; Zeyen

et al., 2015; Pace et al., 2016). Formation of authigenic Fe^{2+}-silicates may have been linked with microbial reduction of Fe^{3+}-minerals (Percak-Dennett et al., 2011). In addition, consortia of ANME and MSR have been shown to facilitate biomineralization of siliceous minerals, some of which contained minor Fe (Chen et al., 2014). These authigenic siliceous Fe^{2+}-minerals may represent the precursors to chlorite and/or quartz associated with Type-A OM. Furthermore, sulfide ions would have been able to react with Fe^{2+} sequestered in minerals such as Fe-phosphates, Fe-carbonates (Egger et al., 2016), or reactive Fe-silicates (Canfield et al., 1992). In turn, the low abundance of organic sulfur in Type-A OM may be explained by preferential reaction of sulfide ions with soluble and/or mineral iron rather than with OM (Werne et al., 2004; Lepot et al., 2009a). In the micro-environments associated with Type-A OM, after depletion of sulfate (Sivan et al., 2011; Egger et al., 2016), Fe^{3+}-minerals may have promoted Fe-dependent AOM both directly and indirectly. The reduction of Fe^{3+}-minerals can fuel Fe-dependent AOM without S (Beal et al., 2009; Egger et al., 2015; Bar-Or et al., 2017). Additionally, a "cryptic sulfur cycle" whereby the abiotic reaction between Fe^{3+}-minerals and HS^- forms S^0 (Fig. 1M) can fuel sulfur-dependent AOM after the direct oxidation of the product S^0 by MSR or after disproportionation of S^0 into HS^- and sulfate (Sivan et al., 2014; Hansel et al., 2015).

Fe-isotope analyses are consistent with intense biogeochemical cycling, indicating that at least some of the pyrite in the Tumbiana stromatolites was formed following the reduction of ferric (oxyhydro)oxides (Nishizawa et al., 2010; Yoshiya et al., 2012). The association of pyrite with $\delta^{56}Fe$ values lower than -3.1 ‰ and OM with $\delta^{13}C_{org}$ values ranging between -51.8 and -40 ‰ has been also used to argue for Fe-dependent AOM in mudstones of the Tumbiana Formation (Yoshiya et al., 2012). Similarly, the pyrites in the Tumbiana stromatolites also feature negative $\delta^{56}Fe$ values (Yoshiya et al., 2012) that may represent either abiotic (Guilbaud et al., 2011) or microbial (Czaja et al., 2012) Fe-reduction processes. The bulk $\delta^{34}S$ values of pyrites are equally equivocal, displaying relatively muted fractionations ($\delta^{34}S$ = -5.7 to 2.7 ‰) that can be explained by either abiotic processes or MSR at low sulfate concentrations (Thomazo et al., 2009b). Microscale $\delta^{34}S$ values, however, display a wide range (-33.7 to +50 ‰) suggesting that sulfate may have been abundant at least in microscale niches (Marin-Carbonne et al., 2018). In summary, the available geochemical evidence suggests that Fe-dependent AOM with or without a "cryptic S-cycle", as well as sulfate-dependent AOM, could have been responsible for the Type-A OM preserved in the Tumbiana stromatolites.

6. Conclusions

In the studied stromatolites, indigenous—Type-A and -B—kerogen displayed $\delta^{13}C_{org}$ values ranging between -65.2 and -50.6 ‰ whereas only pyrobitumen, which is likely exogenous, displayed higher values (-48 to -39.1 ‰). With such low $\delta^{13}C_{org}$ values, neither Type-A and -B OM can be directly related to primary photosynthetic or chemoautotrophic biomass. These OM include a significant fraction of carbon that was fixed through consumption of ^{13}C-depleted methane and/or acetate.

Reviewing known biogeochemical pathways and their combinations reveals that $\delta^{13}C_{org}$ values lower than -50 ‰ are difficult to reconcile with acetogenesis fueled only by fermentation. Acetogenesis fueled by abiotic H_2 in addition to fermentative H_2 may theoretically yield lower $\delta^{13}C$ values. However, thermodynamics dictate that H_2 will be consumed preferentially by microbial reductions of Fe^{3+} and sulfate (Hoehler et al., 1998; Madigan et al., 2009). These oxidized species were present during the deposition of the Tumbiana stromatolites (Yoshiya et al., 2012; Marin-Carbonne et al., 2018). The activity of hydrogenotrophic acetogens would thus have required complete termination of MSR and microbial Fe-reduction. However, we show that the two main types of highly ^{13}C-depleted OM are intimately associated with pyrite and/or organic sulfur, which rather point to a strong coupling between sulfur cycling and OM production. In addition, we still lack evidence for abiotic H_2 sources in the Tumbiana Lake system.

Alternatively, the association of extreme ^{13}C-depletion ($\delta^{13}C^*_{org}$ = -65.2 to -52.5 ‰) in Type-B globules with organic sulfur enrichments strongly argues that this OM was derived from biomass produced by sulfate-dependent AOM. Indeed, some of the ANME-2 produce the most extreme ^{13}C-depletions by reducing sulfate to elemental sulfur and polysulfides, which are highly prone to organic matter sulfurization. The less extreme $\delta^{13}C_{org}$ values (-56.1 to -50.6 ‰) recorded in Type-A OM are most parsimoniously interpreted as the result of AOM using various oxidants. Observation of strongly ^{32}S-enriched nanopyrites in Type-A organic matter in another Tumbiana stromatolite (Marin-Carbonne et al., 2018) suggests that AOM coupled to sulfate reduction may similarly have proceeded in micro-environments where Fe^{2+} was available to outcompete OM for sulfur (Lepot et al., 2009a). Type-A OM is frequently associated with Fe-silicates. The latter could have resulted from Fe^{3+}-reduction (like some Tumbiana pyrites: Nishizawa et al., 2010; Yoshiya et al., 2012), which could have sustained AOM. Future microanalyses of $\delta^{13}C_{org}$, $\delta^{34}S$ and $\delta^{56}Fe$ targeting all the OM-types and associated minerals described herein are anticipated to provide a more comprehensive perspective on the complex and cryptic redox cycles that apparently fueled methanotrophy.

The most extreme bulk-OM $\delta^{13}C_{org}$ values lower than -50.2 ‰ are restricted between 2.8 and 2.7 Ga during the Precambrian, and are apparently unique to lacustrine deposits (Flannery et al., 2016). In the conical stromatolites of the Tumbiana Formation, bulk $\delta^{13}C_{org}$ values as high as -15 ‰ are best interpreted as reflecting photosynthetic primary production (Coffey et al., 2013). In the fluvial-lacustrine Tumbiana system, oxygenic and/or anoxygenic photosynthesis could have produced S°/sulfate and Fe^{3+}-minerals. These, together with the photochemical sulfur aerosols (e.g., Zerkle et al., 2012) may have been concentrated by the drainage basins and evaporation of the Tumbiana Lake system. These oxidized S and Fe species could have fueled anaerobic respiration of OM, as well as S- and possibly Fe-dependent methanotrophy. The impact of lacustrine methanotrophy on Neoarchean atmospheric methane concentrations (Thomazo et al., 2009b; Izon et al., 2015) is difficult to address. The $\delta^{13}C_{org}$ > -50.2 ‰ of Neoarchean and Paleoproterozoic marine deposits may record a more limited methanotrophic biomass. Today's (non-anthropogenic) net release of methane to the atmosphere is mostly contributed by continental ecosystems (Reeburgh, 2007), and is limited in marine context thanks to sulfate-dependent AOM (Knittel and Boetius, 2009). Our study suggests that some Archean lacustrine ecosystems may have consumed methane using sulfate, and possibly,

Fe^{3+}. In contrast, methanotrophy may have been less efficient and/or active in marine, ca. 2.7 Ga sediments, which appeared less depleted in ^{13}C (Flannery et al., 2016). Continental ecosystems may have been widespread at about 2.7 Ga (Thomazo et al., 2018), which is the time of the formation of the first supercontinent (Condie and Aster, 2010). In addition, the Tumbiana Formation deposited between two major episodes of eruption of subaerial large igneous provinces (Kump and Barley, 2007), the weathering of which could have sustained luxuriant photosynthesis in soil and fluvio-lacustrine ecosystems (Lalonde and Konhauser, 2015). Ensuing methane production during OM re-mineralization may have fueled persistent AOM in these newly-formed and possibly widespread types of Archean ecosystems until the protracted Neoarchean rise in oxygen confined these anaerobic metabolisms to a more restricted ecological importance.

7. AKNOWLEDGEMENTS

We thank Noriko Kita and Jim Kern (WiscSIMS, UW-Madison) for assistance with SIMS analyses, and Brian Hess (UW-Madison) for expert SIMS mount preparation and polishing. P.P. thanks the Institut de Physique du Globe de Paris, the Institut des Sciences de l'Univers and the Geological Survey of Western Australia for supporting the PDP. Jian Wang (Canadian Light Source) is thanked for help with STXM analyses. P. Recourt (LOG) is thanked for help with SEM. M. Ader (IPGP) is thanked for providing the LGIS-1A standard. M. Delattre (LOG) is thanked for performing elemental analyses of standards. We thank Drs. A. Zerkle (associate editor), G. Izon, and two anonymous reviewers for their constructive comments that helped improve this manuscript significantly. NanoSIMS analyses were performed at the MNHN-INSU-IMPMC national facility in Paris. K.H.W. acknowledges a grant from the National Aeronautics and Space Agency for work performed at the Jet Propulsion Laboratory, California Institute of Technology. Funding was provided by the NASA Astrobiology Institute (NNA13AA94A), the Agence Nationale de la Recherche (ANR eLife2: ANR-10-BLAN-0602 to P.P.), the São Paulo Research Foundation (FAPESP grant 2015/16235-2 to P.P.), and the Agence Nationale de la Recherche (ANR M6fossils: ANR-15-CE31-0003-01 to K.L.). The WiscSIMS Lab is funded by the National Science Foundation, Division of Earth Sciences (1053466, 1355590, 1658823) and the University of Wisconsin–Madison.

8. REFERENCES

Anbar A. D., Duan Y., Lyons T. W., Arnold G. L., Kendall B., Creaser R. A., Kaufman A. J., Gordon G. W., Scott C., Garvin J. and Buick R. (2007) A Whiff of Oxygen Before the Great Oxidation Event? *Science* **317**, 1903–1906. Available at: http://www.sciencemag.org/cgi/doi/10.1126/science.1140325.

Andres M. S., Sumner D. Y., Reid R. P. and Swart P. K. (2006) Isotopic fingerprints of microbial respiration in aragonite from Bahamian stromatolites. *Geology* **34**, 973–976.

Awramik S. M. and Buchheim H. P. (2009) A giant, Late Archean lake system: The Meentheena Member (Tumbiana Formation; Fortescue Group), Western Australia. *Precambrian Res.* **174**, 215–240.

Balch W. E., Schoberth S., Tanner R. S. and Wolfe R. S. (1977) Acetobacterium, a New Genus of Hydrogen-Oxidizing, Carbon Dioxide-Reducing, Anaerobic Bacteria. *Int. J. Syst. Bacteriol.* **27**, 355–361. Available at: http://ijs.microbiologyresearch.org/content/journal/ijsem/10.1099/00207713-27-4-355.

Bar-Or I., Elvert M., Eckert W., Kushmaro A., Vigderovich H., Zhu Q., Ben-Dov E. and Sivan O. (2017) Iron-Coupled Anaerobic Oxidation of Methane Performed by a Mixed Bacterial-Archaeal Community Based on Poorly Reactive Minerals. *Environ. Sci. Technol.*, acs.est.7b03126.

Bartacek J., Zabranska J. and Lens P. N. L. (2007) Developments and constraints in fermentative hydrogen production. *Biofuels, Bioprod. Biorefining* **1**, 201–214.

Beal E. J., House C. H. and Orphan V. J. (2009) Manganese- and Iron-Dependent Marine Methane Oxidation. *Science* **325**, 184–187.

Beal E. J., Claire M. W. and House C. H. (2011) High rates of anaerobic methanotrophy at low sulfate concentrations with implications for past and present methane levels. *Geobiology* **9**, 131–139.

Birgel D., Meister P., Lundberg R., Horath T. D., Bontognali T. R. R., Bahniuk A. M., de Rezende C. E., Vasconcelos C. and Mckenzie J. A. (2015) Methanogenesis produces strong ^{13}C enrichment in stromatolites of Lagoa Salgada, Brazil: A modern analogue for Palaeo-/Neoproterozoic stromatolites? *Geobiology* **13**, 245–266.

Blake T. S., Buick R., Brown S. J. A. and Barley M. E. (2004) Geochronology of a Late Archaean flood basalt province in the Pilbara Craton, Australia: Constraints on basin evolution, volcanic and sedimentary accumulation, and continental drift rates. *Precambrian Res.* **133**, 143–173.

Blaser M. B., Dreisbach L. K. and Conrad R. (2013) Carbon isotope fractionation of 11 acetogenic strains grown on H2 and CO2. *Appl. Environ. Microbiol.* **79**, 1787–1794.

Boetius A., Ravenschlag K., Schubert C. J., Rickert D., Widdel F., Gieseke A., Amann R., Jørgensen B. B., Witte U. and Pfannkuche O. (2000) A marine microbial consortium apparently mediating anaerobic oxidation of methane. *Nature* **407**, 623–626.

Bolhar R. and Van Kranendonk M. J. (2007) A non-marine depositional setting for the northern

Fortescue Group, Pilbara Craton, inferred from trace element geochemistry of stromatolitic carbonates. *Precambrian Res.* **155**, 229–250.

Bontognali T. R. R., Sessions A. L., Allwood A. C., Fischer W. W., Grotzinger J. P., Summons R. E. and Eiler J. M. (2012) Sulfur isotopes of organic matter preserved in 3.45-billion-year-old stromatolites reveal microbial metabolism. *P. Natl. Acad. Sci. USA* **109**, 15146–15151. Available at: http://www.pnas.org/cgi/doi/10.1073/pnas.1207491109.

Bosak T., Knoll A. H. and Petroff A. P. (2013) The Meaning of Stromatolites. *Annu. Rev. Earth Planet. Sci.* **41**, 21–44. Available at: http://www.annualreviews.org/doi/10.1146/annurev-earth-042711-105327.

Botz R., Pokojski H.-D. D., Schmitt M. and Thomm M. (1996) Carbon isotope fractionation during bacterial methanogenesis by CO2 reduction. *Org. Geochem.* **25**, 255–262.

Buick R. (1992) The antiquity of oxygenic photosynthesis: evidence from stromatolites in sulphate-deficient Archaean lakes. *Science* **255**, 74–77. Available at: http://www.sciencemag.org/cgi/doi/10.1126/science.11536492.

Buick R., Rasmussen B. and Krapez B. (1998) Archean Oil: Evidence for Extensive Hydrocarbon Generation and Migration 2.5–3.5 Ga 1. *Am. Assoc. Pet. Geol. Bull.* **1**, 50–69.

Burne R. V., Moore L. S., Christy A. G., Troitzsch U., King P. L., Carnerup A. M. and Joseph Hamilton P. (2014) Stevensite in the modern thrombolites of Lake Clifton, Western Australia: A missing link in microbialite mineralization? *Geology* **42**, 575–578.

Busigny V., Marin-Carbonne J., Muller E., Cartigny P., Rollion-Bard C., Assayag N. and Philippot P. (2017) Iron and sulfur isotope constraints on redox conditions associated with the 3.2 Ga barite deposits of the Mapepe Formation (Barberton Greenstone Belt, South Africa). *Geochim. Cosmochim. Acta* **210**, 247–266. Available at: http://linkinghub.elsevier.com/retrieve/pii/S0016703717302661.

Canfield D. E., Raiswell R. and Bottrell S. (1992) The reactivity of sedimentary iron minerals toward sulfide. *Am. J. Sci.* **292**, 659–683.

Carignan J., Hild P., Mevelle G., Morel J. and Yeghicheyan D. (2001a) Routine Analyses of Trace Elements in Geological Samples using Flow Injection and Low Pressure On-Line Liquid Chromatography Coupled to ICP-MS: A Study of Geochemical Reference Materials BR, DR-N, UB-N, AN-G and GH. *Geostand. Geoanalytical Res.* **25**, 187–198. Available at: http://doi.wiley.com/10.1111/j.1751-908X.2001.tb00595.x.

Catling D. C. (2006) Comment on "A Hydrogen-Rich Early Earth Atmosphere." *Science* **311**, 38a–38a. Available at: http://www.sciencemag.org/cgi/doi/10.1126/science.1117827.

Chen Y., Li Y. L., Zhou G. T., Li H., Lin Y. T., Xiao X. and Wang F. P. (2014) Biomineralization mediated by anaerobic methane-consuming cell consortia. *Sci. Rep.* **4**, 1–9.

Chung J., Li X. and Rittmann B. E. (2006) Bio-reduction of arsenate using a hydrogen-based membrane biofilm reactor. *Chemosphere* **65**, 24–34. Available at: http://linkinghub.elsevier.com/retrieve/pii/S0045653506003109.

Close H. G., Bovee R. and Pearson A. (2011) Inverse carbon isotope patterns of lipids and kerogen record heterogeneous primary biomass. *Geobiology* **9**, 250–265.

Coffey J. M., Flannery D. T., Walter M. R. and George S. C. (2013) Sedimentology, stratigraphy and geochemistry of a stromatolite biofacies in the 2.72 Ga Tumbiana Formation, Fortescue Group, Western Australia. *Precambrian Res.* **236**, 282–296. Available at: http://dx.doi.org/10.1016/j.precamres.2013.07.021.

Condie K. C. and Aster R. C. (2010) Episodic zircon age spectra of orogenic granitoids: The supercontinent connection and continental growth. *Precambrian Res.* **180**, 227–236.

Conrad R., Claus P., Chidthaisong A., Lu Y., Fernandez Scavino A., Liu Y., Angel R., Galand P. E., Casper P., Guerin F. and Enrich-Prast A. (2014) Stable carbon isotope biogeochemistry of propionate and acetate in methanogenic soils and lake sediments. *Org. Geochem.* **73**, 1–7.

Crowe S. A., Dossing L. N., Beukes N. J., Bau M., Kruger S. J., Frei R. and Canfield D. E. (2013) Atmospheric oxygenation three billion years ago. *Nature* **501**, 535.

Crowe S. A., Paris G., Katsev S., Jones C., Kim S.-T., Zerkle A. L., Nomosatryo S., Fowle D. A., Adkins J. F., Sessions A. L., Farquhar J. and Canfield D. E. (2014) Sulfate was a trace constituent of Archean seawater. *Science* **346**, 735–739. Available at: http://www.sciencemag.org/cgi/doi/10.1126/science.1258966.

Czaja A. D., Johnson C. M., Yamaguchi K. E. and Beard B. L. (2012) Comment on "Abiotic pyrite formation produces a large Fe isotope fractionation". *Science* **335**, 538.

Dauphas N., John S. G. and Rouxel O. (2017) Iron Isotope Systematics. *Rev. Mineral. Geochemistry* **82**, 415–510. Available at: http://rimg.geoscienceworld.org/lookup/doi/10.2138/rmg.2017.82.11.

Deloule E., France-Lanord C. and Albarede F. (1991) D/H analysis of minerals by ion probe. *Stable Isot. Geochemistry A Tribute to Samuel Epstein* **3**, 53–62.

Deloule E. and Robert F. (1995) Interstellar water in meteorites? *Geochim. Cosmochim. Acta* **59**, 4695–4706.

Drake H. L., Küsel K. and Matthies C. (2006) Acetogenic Prokaryotes. In *The Prokaryotes* Springer New York, New York, NY. pp. 354–420. Available at: http://link.springer.com/10.1007/0-387-30742-7_13.

Dupraz C., Reid R. P., Braissant O., Decho A. W., Norman R. S. and Visscher P. T. (2009) Processes of carbonate precipitation in modern microbial mats. *Earth-Science Rev.* **96**, 141–162. Available at: http://dx.doi.org/10.1016/j.earscirev.2008.10.005.

Egger M., Rasigraf O., Sapart C. J., Jilbert T., Jetten M. S. M., Röckmann T., Van Der Veen C., Bânda N., Kartal B., Ettwig K. F. and Slomp C. P. (2015) Iron-mediated anaerobic oxidation of methane in brackish coastal sediments. *Environ. Sci. Technol.* **49**, 277–283.

Egger M., Kraal P., Jilbert T., Sulu-Gambari F., Sapart C. J., Röckmann T. and Slomp C. P. (2016) Anaerobic oxidation of methane alters sediment records of sulfur, iron and phosphorus in the Black Sea. *Biogeosciences* **13**, 5333–5355.

Eigenbrode J. L. and Freeman K. H. (2006) Late Archean rise of aerobic microbial ecosystems. *P. Natl. Acad. Sci. USA* **103**, 15759–15764.

Eigenbrode J. L., Freeman K. H. and Summons R. E. (2008) Methylhopane biomarker hydrocarbons in Hamersley Province sediments provide evidence for Neoarchean aerobiosis. *Earth Planet. Sci. Lett.* **273**, 323–331.

Etique M., Jorand F. P. A. and Ruby C. (2016) Magnetite as a precursor for green rust through the hydrogenotrophic activity of the iron-reducing bacteria Shewanella putrefaciens. *Geobiology* **14**, 237–254. Available at: http://doi.wiley.com/10.1111/gbi.12170.

Ettwig K. F., Shima S., van de Pas-Schoonen K. T., Kahnt J., Medema M. H., op den Camp H. J. M., Jetten M. S. M. and Strous M. (2008) Denitrifying bacteria anaerobically oxidize methane in the absence of Archaea. *Environ. Microbiol.* **10**, 3164–3173. Available at: http://doi.wiley.com/10.1111/j.1462-2920.2008.01724.x.

Farquhar J., Bao H. M. and Thiemens M. (2000) Atmospheric influence of Earth's earliest sulfur cycle. *Science* **289**, 756–758.

Farquhar J., Savarino J., Airieau S. and Thiemens M. H. (2001) Observation of wavelength-sensitive mass-independent sulfur isotope effects during SO2 photolysis: Implications for the early atmosphere. *J. Geophys. Res. Planets* **106**, 32829–32839. Available at: http://doi.wiley.com/10.1029/2000JE001437.

Farquhar J., Cliff J., Zerkle A. L., Kamyshny A., Poulton S. W., Claire M., Adams D. and Harms B. (2013) Pathways for Neoarchean pyrite formation constrained by mass-independent sulfur isotopes. *P. Natl. Acad. Sci. USA* **110**, 17638–17643. Available at: http://www.pnas.org/cgi/doi/10.1073/pnas.1218851110.

Fischer W. W., Fike D. A., Johnson J. E., Raub T. D., Guan Y., Kirschvink J. L. and Eiler J. M. (2014) SQUID-SIMS is a useful approach to uncover primary signals in the Archean sulfur cycle. *P. Natl. Acad. Sci. USA* **111**, 5468–5473. Available at: http://www.pnas.org/cgi/doi/10.1073/pnas.1322577111.

Fischer W. W., Hemp J. and Johnson J. E. (2016) Evolution of Oxygenic Photosynthesis. *Annu. Rev. Earth Planet. Sci.* **44**, 647–683. Available at: http://www.annualreviews.org/doi/10.1146/annurev-earth-060313-054810.

Flannery D. T. and Walter M. R. (2012) Archean tufted microbial mats and the Great Oxidation Event: New insights into an ancient problem. *Aust. J. Earth Sci.* **59**, 1–11.

Flannery D. T., Allwood A. C. and Van Kranendonk M. J. (2016) Lacustrine facies dependence of highly 13C-depleted organic matter during the global age of methanotrophy. *Precambrian Res.* **285**, 216–241. Available at: http://dx.doi.org/10.1016/j.precamres.2016.09.021.

Fleet M. E. (2005) XANES spectroscopy of sulfur in Earth materials. *Can. Mineral.* **43**, 1811–1838.

Frei R., Gaucher C., Poulton S. W. and Canfield D. E. (2009) Fluctuations in Precambrian atmospheric oxygenation recorded by chromium isotopes. *Nature* **461**, 250–253. Available at: http://www.nature.com/doifinder/10.1038/nature08266.

French K. L., Hallmann C., Hope J. M., Schoon P. L., Zumberge J. A., Hoshino Y., Peters C. A., George S. C., Love G. D., Brocks J. J., Buick R. and Summons R. E. (2015) Reappraisal of hydrocarbon biomarkers in Archean rocks. *P. Natl. Acad. Sci. USA* **112**, 5915–5920. Available at: http://www.pnas.org/content/112/19/5915.abstract.

Freude C. and Blaser M. (2016) Carbon isotope fractionation during catabolism and anabolism in acetogenic bacteria growing on different substrates. *Appl. Environ. Microbiol.* **82**, 2728–2737.

Garvin J., Buick R., Anbar A. D., Arnold G. L. and Kaufman A. J. (2009) Isotopic Evidence for an Aerobic Nitrogen Cycle in the Latest Archean. *Science* **323**, 1045–1048. Available at: http://www.sciencemag.org/cgi/doi/10.1126/science.1165675.

Gelwicks J. T., Risatti J. B. and Hayes J. M. (1989) Carbon isotope effects associated with autotrophic acetogenesis. *Org. Geochem.* **14**, 441–6.

Ghosh W. and Dam B. (2009) Biochemistry and molecular biology of lithotrophic sulfur oxidation by taxonomically and ecologically diverse bacteria and archaea. *FEMS Microbiol. Rev.* **33**, 999–1043.

Goevert D. and Conrad R. (2008) Carbon Isotope Fractionation by Sulfate-Reducing Bacteria Using Different Pathways for the Oxidation of Acetate. *Environ. Sci. Technol.* **42**, 7813–7817. Available at: http://pubs.acs.org/doi/abs/10.1021/es800308z.

Goevert D. and Conrad R. (2009) Effect of substrate concentration on carbon isotope fractionation during acetoclastic methanogenesis by Methanosarcina barkeri and M. acetivorans and in rice field soil. *Appl. Environ. Microbiol.* **75**, 2605–2612.

Grassineau N. V., Nisbet E. G., Fowler C. M. R., Bickle M. J., Lowry D., Chapman H. J., Mattey D. P., Abell P., Yong J. and Martin a. (2002) Stable isotopes in the Archaean Belingwe belt, Zimbabwe: evidence for a diverse microbial mat ecology. *Geol. Soc. London, Spec. Publ.* **199**, 309–328.

Greinert J., Bohrmann G. and Elvert M. (2002) Stromatolitic fabric of authigenic carbonate crusts: Result of anaerobic methane oxidation at cold seeps in 4,850 m water depth. *Int. J. Earth Sci.* **91**, 698–711.

Guilbaud R., Butler I. B. and Ellam R. M. (2011) Abiotic pyrite formation produces a large Fe isotope fractionation. *Science* **332**, 1548–1551.

Guo Q., Strauss H., Kaufman A. J., Schröder S., Gutzmer J., Wing B., Baker M. A., Bekker A., Jin Q., Kim S. T. and Farquhar J. (2009) Reconstructing Earth's surface oxidation across the Archean-Proterozoic transition. *Geology* **37**, 399–402.

Hansel C. M., Lentini C. J., Tang Y., Johnston D. T., Wankel S. D. and Jardine P. M. (2015) Dominance of sulfur-fueled iron oxide reduction in low-sulfate freshwater sediments. *ISME J.* **9**, 2400–2412. Available at: http://dx.doi.org/10.1038/ismej.2015.50.

Hanson R. S. and Hanson T. E. (1996) Methanotrophic bacteria. *Microbiol. Rev.* **60**, 439–471.

Haroon M. F., Hu S., Shi Y., Imelfort M., Keller J., Hugenholtz P., Yuan Z. and Tyson G. W. (2013) Anaerobic oxidation of methane coupled to nitrate reduction in a novel archaeal

lineage. *Nature* **500**, 567–570. Available at: http://dx.doi.org/10.1038/nature12375.

Hayes J. M. (1994) Global methanotrophy of the Archean-Proterozoic transition. In *Early life on earth, Nobel Symposium No. 84* (ed. S. Bengtson). Columbia University Press, New York. pp. 220–235.

Hayes J. M., Kaplan I. R. and Wedeking K. W. (1983) Precambrian organic geochemistry, preservation of the record. In *The Earth's earliest biosphere* (ed. J. W. Schopf). Princeton University Press, Princeton, New Jersey. pp. 93–134.

Heuer V. B., Pohlman J. W., Torres M. E., Elvert M. and Hinrichs K.-U. (2009) The stable carbon isotope biogeochemistry of acetate and other dissolved carbon species in deep subseafloor sediments at the northern Cascadia Margin. *Geochim. Cosmochim. Acta* **73**, 3323–3336. Available at: http://linkinghub.elsevier.com/retrieve/pii/S0016703709001331.

Heuer V. B., Krüger M., Elvert M. and Hinrichs K.-U. (2010) Experimental studies on the stable carbon isotope biogeochemistry of acetate in lake sediments. *Org. Geochem.* **41**, 22–30. Available at: http://linkinghub.elsevier.com/retrieve/pii/S0146638009001557.

Hinrichs K. U. (2002) Microbial fixation of methane carbon at 2.7 Ga: Was an anaerobic mechanism possible? *Geochemistry Geophys. Geosystems* **3**, 1042.

Hinrichs K.-U., Summons R. E., Orphan V., Sylva S. P. and Hayes J. M. (2000) Molecular and isotopic analysis of anaerobic methane-oxidizing communities in marine sediments. *Org. Geochem.* **31**, 1685–1701.

Hoehler T. M., Alperin M. J., Albert D. B. and Martens C. S. (1998) Thermodynamic control on hydrogen concentrations in anoxic sediments. *Geochim. Cosmochim. Acta* **62**, 1745–1756.

Hofmann H. J. (2000) Archean Stromatolites as Microbial Archives. In *Microbial Sediments* (eds. R. E. Riding and S. M. Awramik). Springer Berlin Heidelberg, Berlin, Heidelberg. pp. 315–327. Available at: http://link.springer.com/10.1007/978-3-662-04036-2_34.

House C. H., Schopf J. W., McKeegan K. D., Coath C. D., Harrison T. M. and Stetter K. O. (2000) Carbon isotopic composition of individual Precambrian microfossils. *Geology* **28**, 707–710.

House C. H., Schopf J. W. and Stetter K. O. (2003) Carbon isotopic fractionation by Archaeans and other thermophilic prokaryotes. *Org. Geochem.* **34**, 345–356.

Izon G., Zerkle A. L., Zhelezinskaia I., Farquhar J., Newton R. J., Poulton S. W., Eigenbrode J. L. and Claire M. W. (2015) Multiple oscillations in Neoarchaean atmospheric chemistry. *Earth Planet. Sci. Lett.* **431**, 264–273. Available at: http://dx.doi.org/10.1016/j.epsl.2015.09.018.

Izon G., Zerkle A. L., Williford K. H., Farquhar J., Poulton S. W. and Claire M. W. (2017) Biological regulation of atmospheric chemistry en route to planetary oxygenation. *P. Natl. Acad. Sci. USA* **114**, E2571–E2579. Available at: http://www.pnas.org/lookup/doi/10.1073/pnas.1618798114.

Jacobsen C., Wirick S., Flynn G. and Zimba C. (2000) Soft X-ray spectroscopy from image sequences with sub-100 nm spatial resolution. *J. Microsc.* **197**, 173–184.

Johnston D. T. (2011) Multiple sulfur isotopes and the evolution of Earth ' s surface sulfur cycle. *Earth Sci. Rev.* **106**, 161–183. Available at: http://dx.doi.org/10.1016/j.earscirev.2011.02.003.

Jones C. and Crowe S. A. (2013) No evidence for manganese-oxidizing photosynthesis. *P. Natl. Acad. Sci. USA* **110**, E4118–E4118. Available at: http://www.pnas.org/cgi/doi/10.1073/pnas.1314380110.

Kamber B. S. and Whitehouse M. J. (2006) Micro-scale sulphur isotope evidence for sulphur cycling in the late Archean shallow ocean. *Geobiology* **5**, 5–17. Available at: http://doi.wiley.com/10.1111/j.1472-4669.2006.00091.x.

Kaufman A. J. and Xiao S. (2003) High CO2 levels in the Proterozoic atmosphere estimated from analyses of individual microfossils. *Nature* **425**, 279–282. Available at: http://www.nature.com/doifinder/10.1038/nature01902.

Kaznatcheev K. V., Karunakaran C., Lanke U. D., Urquhart S. G., Obst M. and Hitchcock A. P. (2007) Soft X-ray spectromicroscopy beamline at the CLS: Commissioning results. *Nucl. Instruments Methods Phys. Res. Sect. A Accel. Spectrometers, Detect. Assoc. Equip.* **582**, 96–99.

Kendall B., Dahl T. W. and Anbar A. D. (2017) The stable isotope geochemistry of Molybdenum. *Rev. Mineral. Geochemistry* **82**, 683–732. Available at: http://rimg.geoscienceworld.org/lookup/doi/10.2138/rmg.2017.82.16.

Klueglein N., Zeitvogel F., Stierhof Y. D., Floetenmeyer M., Konhauser K. O., Kappler A. and Obst M. (2014) Potential role of nitrite for abiotic Fe(II) oxidation and cell encrustation during nitrate reduction by denitrifying bacteria. *Appl. Environ. Microbiol.* **80**, 1051–1061.

Knittel K. and Boetius A. (2009) Anaerobic Oxidation of Methane: Progress with an Unknown Process. *Annu. Rev. Microbiol.* **63**, 311–334. Available at: http://www.annualreviews.org/doi/10.1146/annurev.micro.61.080706.093130.

Konhauser K. O. (2007) *Introduction to Geomicrobiology*. Wiley-Blackwell, Oxford.

Konn C., Charlou J. L., Holm N. G. and Mousis O. (2015) The Production of Methane, Hydrogen, and Organic Compounds in Ultramafic-Hosted Hydrothermal Vents of the Mid-Atlantic Ridge. *Astrobiology* **15**, 381–399. Available at: http://online.liebertpub.com/doi/10.1089/ast.2014.1198.

Kopp R. E., Kirschvink J. L., Hilburn I. A. and Nash C. Z. (2005) The Paleoproterozoic snowball Earth: A climate disaster triggered by the evolution of oxygenic photosynthesis. *P. Natl. Acad. Sci. USA* **102**, 11131–11136. Available at: http://www.pnas.org/cgi/doi/10.1073/pnas.0504878102.

Krause S., Aloisi G., Engel A., Liebetrau V. and Treude T. (2014) Enhanced Calcite Dissolution in the Presence of the Aerobic Methanotroph Methylosinus trichosporium. *Geomicrobiol. J.* **31**, 325–337.

Kump L. R. and Barley M. E. (2007) Increased subaerial volcanism and the rise of atmospheric oxygen 2.5 billion years ago. *Nature* **448**, 1033–1036.

Kurzweil F., Claire M., Thomazo C., Peters M., Hannington M. and Strauss H. (2013) Atmospheric sulfur rearrangement 2.7 billion years ago: Evidence for oxygenic photosynthesis. *Earth Planet. Sci. Lett.* **366**, 17–26. Available at: http://dx.doi.org/10.1016/j.epsl.2013.01.028.

Lalonde S. V. and Konhauser K. O. (2015) Benthic perspective on Earth's oldest evidence for oxygenic photosynthesis. *P. Natl. Acad. Sci. USA* **112**, 995–1000. Available at: http://www.pnas.org/lookup/doi/10.1073/pnas.1415718112.

Lepot K., Benzerara K., Brown G. E. and Philippot P. (2008) Microbially influenced formation of 2,724-million-year-old stromatolites. *Nat. Geosci.* **1**, 118–121. Available at: http://www.nature.com/doifinder/10.1038/ngeo107.

Lepot K., Benzerara K., Rividi N., Cotte M., Brown G. E. and Philippot P. (2009a) Organic matter heterogeneities in 2.72 Ga stromatolites: Alteration versus preservation by sulfur incorporation. *Geochim. Cosmochim. Acta* **73**, 6579–6599. Available at: https://doi.org/10.1016/j.gca.2009.08.014.

Lepot K., Philippot P., Benzerara K. and Wang G. Y. (2009b) Garnet-filled trails associated with carbonaceous matter mimicking microbial filaments in Archean basalt. *Geobiology* **7**, 393–402. Available at: https://doi.org/10.1111/j.1472-4669.2009.00208.x.

Lepot K., Benzerara K. and Philippot P. (2011) Biogenic versus metamorphic origins of diverse microtubes in 2.7Gyr old volcanic ashes: Multi-scale investigations. *Earth Planet. Sci. Lett.* **312**, 37–47. Available at: https://doi.org/10.1016/j.epsl.2011.10.016.

Lepot K., Williford K. H., Ushikubo T., Sugitani K., Mimura K., Spicuzza M. J. and Valley J. W. (2013) Texture-specific isotopic compositions in 3.4 Gyr old organic matter support selective preservation in cell-like structures. *Geochim. Cosmochim. Acta* **112**, 66–86. Available at: https://doi.org/10.1016/j.gca.2013.03.004.

Lepot K., Compère P., Gérard E., Namsaraev Z., Verleyen E., Tavernier I., Hodgson D. A., Vyverman W., Gilbert B., Wilmotte A. and Javaux E. J. (2014) Organic and mineral imprints in fossil photosynthetic mats of an East Antarctic lake. *Geobiology* **12**, 424–450. Available at: https://doi.org/10.1111/gbi.12096.

Leventhal J. S. and Threlkeld C. N. (1978) Carbon-13/Carbon-12 Isotope Fractionation of Organic Matter Associated with Uranium Ores Induced by Alpha Irradiation. *Science* **202**, 430–432. Available at: http://www.sciencemag.org/cgi/doi/10.1126/science.202.4366.430.

Li W., Czaja A. D., Van Kranendonk M. J., Beard B. L., Roden E. E. and Johnson C. M. (2013) An anoxic, Fe(II)-rich, U-poor ocean 3.46 billion years ago. *Geochim. Cosmochim. Acta* **120**, 65–79.

Liu D., Dong Hailiang H., Bishop M. E., Wang H., Agrawal A., Tritschler S., Eberl D. D. and Xie S. (2011) Reduction of structural Fe(III) in nontronite by methanogen Methanosarcina barkeri. *Geochim. Cosmochim. Acta* **75**, 1057–1071. Available at: http://dx.doi.org/10.1016/j.gca.2010.11.009.

Londry K. L. and Des Marais D. J. (2003) Stable carbon isotope fractionation by sulfate-reducing bacteria. *Appl. Environ. Microbiol.* **69**, 2942–9. Available at:

http://www.pubmedcentral.nih.gov/articlerender.fcgi?artid=154509&tool=pmcentrez&rendertype=abstract.

Londry K. L., Dawson K. G., Grover H. D., Summons R. E. and Bradley A. S. (2008) Stable carbon isotope fractionation between substrates and products of Methanosarcina barkeri. *Org. Geochem.* **39**, 608–621.

Lovley D. R. (1991) Dissimilatory Fe (III) and Mn (IV) reduction. *Microbiol. Rev.* **55**, 259–287.

Luo G., Ono S., Beukes N. J., Wang D. T., Xie S. and Summons R. E. (2016) Rapid oxygenation of Earth's atmosphere 2.33 billion years ago. *Sci. Adv.* **2**, 1–10.

Luo G., Junium C. K., Izon G., Ono S., Beukes N. J., Algeo T. J., Cui Y., Xie S. and Summons R. E. (2018) Nitrogen fixation sustained productivity in the wake of the Palaeoproterozoic Great Oxygenation Event. *Nat. Commun.* **9**, 978. Available at: http://dx.doi.org/10.1038/s41467-018-03361-2.

Madigan M. T., Martinko J. M., Benser K. S., Buckley D. H. and Stahl D. A. (2009) *Brock biology of Microorganisms*. Pearson, Glenview.

Des Marais D. J. (2001) Isotopic evolution of the biogeochemical carbon cycle during the Precambrian. In *Reviews In Mineralogy and Geochemistry vol 43: Stable Isotope Geochemistry* (eds. J. W. Valley and D. R. Cole). Mineralogical Society of America. pp. 555–578.

Marin-Carbonne J., Remusat L., Sforna M. C., Thomazo C., Cartigny P. and Philippot P. (2018) Sulfur isotope's signal of nanopyrites enclosed in 2.7 Ga stromatolitic organic remains reveal microbial sulfate reduction. *Geobiology* **16**, 121–138. Available at: http://doi.wiley.com/10.1111/gbi.12275.

Marlow J. J., Steele J. A., Ziebis W., Thurber A. R., Levin L. A. and Orphan V. J. (2014) Carbonate-hosted methanotrophy represents an unrecognized methane sink in the deep sea. *Nat. Commun.* **5**, 5094. Available at: http://www.nature.com/doifinder/10.1038/ncomms6094.

McCollom T. M. and Seewald J. S. (2013) Serpentinites, hydrogen, and life. *Elements* **9**, 129–134.

Mével C. (2003) Serpentinization of abyssal peridotites at mid-ocean ridges. *Comptes Rendus Geosci.* **335**, 825–852. Available at: http://linkinghub.elsevier.com/retrieve/pii/S1631071303001354.

Michaelis W., Seifert R., Nauhaus K., Treude T., Thiel V., Blumenberg M., Knittel K., Gieseke A., Peterknecht K., Pape T., Boetius A., Amann R., Jørgensen B. B., Widdel F., Peckmann J., Pimenov N. V. and Gulin M. B. (2002) Microbial reefs in the black sea fueled by anaerobic oxidation of methane. *Science* **297**, 1013–1015. Available at: http://www.sciencemag.org/cgi/doi/10.1126/science.1072502.

Milucka J., Ferdelman T. G., Polerecky L., Franzke D., Wegener G., Schmid M., Lieberwirth I., Wagner M., Widdel F. and Kuypers M. M. M. (2012) Zero-valent sulphur is a key intermediate in marine methane oxidation. *Nature* **491**, 541–546. Available at: http://dx.doi.org/10.1038/nature11656.

Miot J., Benzerara K., Morin G., Kappler A., Bernard S., Obst M., Férard C., Skouri-Panet F., Guigner J.-M., Posth N., Galvez M., Jr. G. E. B. and Guyot F. (2009) Iron biomineralization by anaerobic neutrophilic iron-oxidizing bacteria. *Geochim. Cosmochim. Acta* **73**, 696–711.

Mole D. R., Barnes S. J., Yao Z., White A. J. R., Maas R. and Kirkland C. L. (2018) The Archean Fortescue large igneous province: A result of komatiite contamination by a distinct Eo-Paleoarchean crust. *Precambrian Res.* **310**, 365–390. Available at: http://linkinghub.elsevier.com/retrieve/pii/S0301926817306757.

Nishizawa M., Yamamoto H., Ueno Y., Tsuruoka S., Shibuya T., Sawaki Y., Yamamoto S., Kon Y., Kitajima K., Komiya T., Maruyama S. and Hirata T. (2010) Grain-scale iron isotopic distribution of pyrite from Precambrian shallow marine carbonate revealed by a femtosecond laser ablation multicollector ICP-MS technique: Possible proxy for the redox state of ancient seawater. *Geochim. Cosmochim. Acta* **74**, 2760–2778. Available at: http://dx.doi.org/10.1016/j.gca.2010.02.014.

Norði K. à., Thamdrup B. and Schubert C. J. (2013) Anaerobic oxidation of methane in an iron-rich Danish freshwater lake sediment. *Limnol. Oceanogr.* **58**, 546–554. Available at: http://doi.wiley.com/10.4319/lo.2013.58.2.0546.

Orphan V. J., House C. H., Hinrichs K. U., McKeegan K. D. and DeLong E. F. (2001) Methane-consuming archaea revealed by directly coupled isotopic and phylogenetic analysis. *Science* **293**, 484–487.

Orphan V. J., House C. H., Hinrichs K.-U., McKeegan K. D. and DeLong E. F. (2002) Multiple archaeal groups mediate methane oxidation in anoxic cold seep sediments. *P. Natl. Acad. Sci. USA* **99**, 7663–7668. Available at: http://www.pnas.org/content/99/11/7663.abstract.

Pace A., Bourillot R., Bouton A., Vennin E., Galaup S., Bundeleva I., Patrier P., Dupraz C., Thomazo C., Sansjofre P., Yokoyama Y., Franceschi M., Anguy Y., Pigot L., Virgone A. and Visscher P. T. (2016) Microbial and diagenetic steps leading to the mineralisation of Great Salt Lake microbialites. *Sci. Rep.* **6**, 31495. Available at: http://www.nature.com/articles/srep31495.

Pavlov A. A. and Kasting J. F. (2002) Mass-Independent Fractionation of Sulfur Isotopes in Archean Sediments: Strong Evidence for an Anoxic Archean Atmosphere. *Astrobiology* **2**, 27–41. Available at: http://www.liebertonline.com/doi/abs/10.1089/153110702753621321.

Pavlov A. A., Kasting J. F., Eigenbrode J. L. and Freeman K. H. (2001) Organic haze in Earth's early atmosphere: Source of low-C-13 Late Archean kerogens? *Geology* **29**, 1003–1006.

Pearson A. (2010) Pathways of carbon assimilation and their impact on organic matter values d13C. In *Handbook of Hydrocarbon and Lipid Microbiology* (ed. K. N. Timmis). Springer-Verlag, Berlin Heidelberg. pp. 143–156. Available at: http://link.springer.com/10.1007/978-3-540-77587-4.

Penning H., Claus P., Casper P. and Conrad R. (2006) Carbon isotope fractionation during acetoclastic methanogenesis by Methanosaeta concilii in culture and a lake sediment. *Appl. Environ. Microbiol.* **72**, 5648–5652.

Penning H. and Conrad R. (2006) Carbon isotope effects associated with mixed-acid fermentation of saccharides by Clostridium papyrosolvens. *Geochim. Cosmochim. Acta* **70**, 2283–2297.

Percak-Dennett E. M., Beard B. L., Xu H., Konishi H., Johnson C. M. and Roden E. E. (2011) Iron isotope fractionation during microbial dissimilatory iron oxide reduction in simulated Archaean seawater. *Geobiology* **9**, 205–220.

Philippot P., Van Zuilen M., Lepot K., Thomazo C., Farquhar J. and Van Kranendonk M. (2007) Early Archaean microorganisms preferred reduced sulfur, not sulfate. *Science* **317**, 1534–1537.

Philippot P., Van Kranendonk M., Van Zuilen M., Lepot K., Rividi N., Teitler Y., Thomazo C., Blanc-Valleron M. M., Rouchy J. M., Grosch E. and de Wit M. (2009) Early traces of life investigations in drilling Archean hydrothermal and sedimentary rocks of the Pilbara Craton, Western Australia and Barberton Greenstone Belt, South Africa. *Comptes Rendus - Palevol* **8**, 649–663. Available at: https://doi.org/10.1016/j.crpv.2009.06.006.

Philippot P., Ávila J. N., Killingsworth B. A., Tessalina S., Baton F., Caquineau T., Muller E., Pecoits E., Cartigny P., Lalonde S. V., Ireland T. R., Thomazo C., Van Kranendonk M. J. and Busigny V. (2018) Globally asynchronous sulphur isotope signals require re-definition of the Great Oxidation Event. *Nat. Commun.* **9**. Available at: http://dx.doi.org/10.1038/s41467-018-04621-x.

Planavsky N. J., Asael D., Hofmann A., Reinhard C. T., Lalonde S. V., Knudsen A., Wang X., Ossa Ossa F., Pecoits E., Smith A. J. B., Beukes N. J., Bekker A., Johnson T. M., Konhauser K. O., Lyons T. W. and Rouxel O. J. (2014) Evidence for oxygenic photosynthesis half a billion years before the Great Oxidation Event. *Nat. Geosci.* **7**, 283–286. Available at: http://www.nature.com/doifinder/10.1038/ngeo2122.

Preuß A., Schauder R., Fuchs G. and Stichler W. (1989) Carbon Isotope Fractionation by Autotrophic Bacteria with Three Different CO2 Fixation Pathways. *Zeitschrift für Naturforsch. C* **44**. Available at: http://www.degruyter.com/view/j/znc.1989.44.issue-5-6/znc-1989-5-610/znc-1989-5-610.xml.

Quijada M., Riboulleau A., Faure P., Michels R. and Tribovillard N. (2016) Organic matter sulfurization on protracted diagenetic timescales: The possible role of anaerobic oxidation of methane. *Mar. Geol.* **381**, 54–66. Available at: http://dx.doi.org/10.1016/j.margeo.2016.08.010.

Raghoebarsing A. A., Pol A., van de Pas-Schoonen K. T., Smolders A. J. P., Ettwig K. F., Rijpstra W. I. C., Schouten S., Damsté J. S. S., Op den Camp H. J. M., Jetten M. S. M. and Strous M. (2006) A microbial consortium couples anaerobic methane oxidation to denitrification. *Nature* **440**, 918–921. Available at: http://www.nature.com/doifinder/10.1038/nature04617.

Rasigraf O., Vogt C., Richnow H.-H., Jetten M. S. M. and Ettwig K. F. (2012) Carbon and hydrogen isotope fractionation during nitrite-dependent anaerobic methane oxidation by Methylomirabilis oxyfera. *Geochim. Cosmochim. Acta* **89**, 256–264. Available at: http://linkinghub.elsevier.com/retrieve/pii/S0016703712002700.

Rasmussen B. (2005) Evidence for pervasive petroleum generation and migration in 3.2 and 2.63 Ga shales. *Geology* **33**, 497–500.

Rasmussen B., Fletcher I. R. and McNaughton N. J. (2001) Dating low-grade metamorphic events by SHRIMP U-Pb analysis of monazite in shales. *Geology* **29**, 963–966.

Rasmussen B., Blake T. S., Fletcher I. R. and Kilburn M. R. (2009) Evidence for microbial life in synsedimentary cavities from 2.75 Ga terrestrial environments. *Geology* **37**, 423–426.

Reeburgh W. S. (2007) Oceanic Methane Biogeochemistry. *Chem. Rev.* **107**, 486–513.

Riboulleau A., Derenne S., Sarret G., Largeau C., Baudin F. and Connan J. (2000) Pyrolytic and spectroscopic study of a sulphur-rich kerogen from the "Kashpir oil shales" (Upper Jurassic, Russian platform). *Org. Geochem.* **31**, 1641–1661.

Roh Y., Gao H., Vali H., Kennedy D. W., Yang Z. K., Gao W., Dohnalkova A. C., Stapleton R. D., Moon J.-W., Phelps T. J., Fredrickson J. K. and Zhou J. (2006) Metal Reduction and Iron Biomineralization by a Psychrotolerant Fe(III)-Reducing Bacterium, Shewanella sp. Strain PV-4. *Appl. Environ. Microbiol.* **72**, 3236–3244. Available at: http://aem.asm.org/cgi/doi/10.1128/AEM.72.5.3236-3244.2006.

Rothman D. H., Fournier G. P., French K. L., Alm E. J., Boyle E. A., Cao C. and Summons R. E. (2014) Methanogenic burst in the end-Permian carbon cycle. *P. Natl. Acad. Sci. USA* **111**, 5462–5467. Available at: http://www.pnas.org/cgi/doi/10.1073/pnas.1318106111.

Sakurai R., Ito M., Ueno Y., Kitajima K. and Maruyama S. (2005) Facies architecture and sequence-stratigraphic features of the Tumbiana Formation in the Pilbara Craton, northwestern Australia: Implications for depositional environments of oxygenic stromatolites during the Late Archean. *Precambrian Res.* **138**, 255–273.

Sangély L., Chaussidon M., Michels R. and Huault V. (2005) Microanalysis of carbon isotope composition in organic matter by secondary ion mass spectrometry. *Chem. Geol.* **223**, 179–195.

Sangély L., Chaussidon M., Michels R., Brouand M., Cuney M., Huault V. and Landais P. (2007) Micrometer scale carbon isotopic study of bitumen associated with Athabasca uranium deposits: Constraints on the genetic relationship with petroleum source-rocks and the abiogenic origin hypothesis. *Earth Planet. Sci. Lett.* **258**, 378–396.

Schoell M. and Wellmer F.-W. (1981) Anomalous 13C depletion in early Precambrian graphites from Superior Province, Canada. *Nature* **290**, 696–699. Available at: http://www.nature.com/doifinder/10.1038/290696a0.

Sforna M. C., Philippot P., Somogyi A., Van Zuilen M. A., Medjoubi K., Schoepp-Cothenet B., Nitschke W. and Visscher P. T. (2014) Evidence for arsenic metabolism and cycling by microorganisms 2.7 billion years ago. *Nat. Geosci.* **7**, 811–815. Available at: http://www.nature.com/doifinder/10.1038/ngeo2276.

Sforna M. C., Daye M., Philippot P., Somogyi A., van Zuilen M. A., Medjoubi K., Gï¿½rard E., Jamme F., Dupraz C., Braissant O., Glunk C. and Visscher P. T. (2017) Patterns of metal distribution in hypersaline microbialites during early diagenesis: Implications for the fossil record. *Geobiology* **15**, 259–279.

Shen Y., Farquhar J., Masterson A., Kaufman A. J. and Buick R. (2009) Evaluating the role of

microbial sulfate reduction in the early Archean using quadruple isotope systematics. *Earth Planet. Sci. Lett.* **279**, 383–391. Available at: http://dx.doi.org/10.1016/j.epsl.2009.01.018.

Sim M. S., Liang B., Petroff A. P., Evans A., Klepac-Ceraj V., Flannery D. T., Walter M. R. and Bosak T. (2012) Oxygen-Dependent Morphogenesis of Modern Clumped Photosynthetic Mats and Implications for the Archean Stromatolite Record. *Geosciences* **2**, 235–259. Available at: http://www.mdpi.com/2076-3263/2/4/235/.

Sivan O., Adler M., Pearson A., Gelman F., Bar-Or I., John S. G. and Eckert W. (2011) Geochemical evidence for iron-mediated anaerobic oxidation of methane. *Limnol. Oceanogr.* **56**, 1536–1544. Available at: http://doi.wiley.com/10.4319/lo.2011.56.4.1536.

Sivan O., Antler G., Turchyn A. V., Marlow J. J. and Orphan V. J. (2014) Iron oxides stimulate sulfate-driven anaerobic methane oxidation in seeps. *P. Natl. Acad. Sci. USA* **111**, E4139–E4147. Available at: http://www.pnas.org/lookup/doi/10.1073/pnas.1412269111.

Slotznick S. P. and Fischer W. W. (2016) Examining Archean methanotrophy. *Earth Planet. Sci. Lett.* **441**, 52–59. Available at: http://dx.doi.org/10.1016/j.epsl.2016.02.013.

Smith R. E., Perdrix J. L. and Parks T. C. (1982) Burial metamorphism in the Hamersley basin, Western Australia. *J. Petrol.* **23**, 75–102.

Spool A. M. (2004) Interpretation of static secondary ion spectra. *Surf. Interface Anal.* **36**, 264–274.

Strauss H. and Moore T. B. (1992) Abundances and Isotopic compositions of Carbon and Sulfur species in Whole rock and Kerogen samples. In *The Proterozoic Biosphere: A Multidisciplinary Study* (eds. J. W. Schopf and C. Klein). Cambridge University Press. pp. 709–798.

Strauss H., Des Marais D. J., Summons R. E. and Hayes. J. (1992) The carbon isotopic record. In *The Proterozoic biosphere: A multidisciplinary study* (eds. J. W. Schopf and C. Klein). Cambridge.

Stüeken E. E., Buick R. and Anbar A. D. (2015a) Selenium isotopes support free O2 in the latest Archean. *Geology* **43**, 259–262.

Stüeken E. E., Buick R. and Schauer A. J. (2015b) Nitrogen isotope evidence for alkaline lakes on late Archean continents. *Earth Planet. Sci. Lett.* **411**, 1–10. Available at: http://dx.doi.org/10.1016/j.epsl.2014.11.037.

Stüeken E. E., Buick R., Anderson R. E., Baross J. A., Planavsky N. J. and Lyons T. W. (2017) Environmental niches and metabolic diversity in Neoarchean lakes. *Geobiology* **15**, 767–783.

Summons R. E., Jahnke L. L. and Roksandic Z. (1994) Carbon isotopic fractionation in lipids from methanotrophic bacteria: Relevance for interpretation of the geochemical record of biomarkers. *Geochim. Cosmochim. Acta* **58**, 2853–2863. Available at: http://linkinghub.elsevier.com/retrieve/pii/0016703794901198.

Templeton A. S., Chu K. H., Alvarez-Cohen L. and Conrad M. E. (2006) Variable carbon isotope fractionation expressed by aerobic CH4-oxidizing bacteria. *Geochim. Cosmochim. Acta* **70**, 1739–1752.

Thomazo C., Pinti D. L., Busigny V., Ader M., Hashizume K. and Philippot P. (2009a) Biological activity and the Earth's surface evolution: Insights from carbon, sulfur, nitrogen and iron stable isotopes in the rock record. *Comptes Rendus Palevol* **8**, 665–678. Available at: http://linkinghub.elsevier.com/retrieve/pii/S163106830900102X.

Thomazo C., Ader M., Farquhar J. and Philippot P. (2009b) Methanotrophs regulated atmospheric sulfur isotope anomalies during the Mesoarchean (Tumbiana Formation, Western Australia). *Earth Planet. Sci. Lett.* **279**, 65–75. Available at: http://linkinghub.elsevier.com/retrieve/pii/S0012821X08007930.

Thomazo C., Ader M. and Philippot P. (2011) Extreme15N-enrichments in 2.72-Gyr-old sediments: Evidence for a turning point in the nitrogen cycle. *Geobiology* **9**, 107–120.

Thomazo C., Nisbet E. G., Grassineau N. V., Peters M. and Strauss H. (2013) Multiple sulfur and carbon isotope composition of sediments from the Belingwe Greenstone Belt (Zimbabwe): A biogenic methane regulation on mass independent fractionation of sulfur during the Neoarchean? *Geochim. Cosmochim. Acta* **121**, 120–138. Available at: http://dx.doi.org/10.1016/j.gca.2013.06.036.

Thomazo C., Couradeau E. and Garcia-Pichel F. (2018) Possible nitrogen fertilization of the early Earth Ocean by microbial continental ecosystems. *Nat. Commun.* **9**, 2530. Available at: http://www.nature.com/articles/s41467-018-04995-y.

Thomen A., Robert F. and Remusat L. (2014) Determination of the nitrogen abundance in organic materials by NanoSIMS quantitative imaging. *J. Anal. At. Spectrom.* **29**, 512. Available at: http://xlink.rsc.org/?DOI=c3ja50313e.

Thorne A. M. and Trendall A. F. (2001) Geology of the Fortescue Group, Pilbara Craton, Western Australia. *Bull. Geol. Surv. West. Aust.* **144**, 1–249.

Tian F. (2005) A Hydrogen-Rich Early Earth Atmosphere. *Science* **308**, 1014–1017. Available at: http://www.sciencemag.org/cgi/doi/10.1126/science.1106983.

Tourillon G., Mahatsekake C., Andrieu C., Williams G. P., Garrett R. F. and Braun W. (1988) Electronic structure and orientation studies of undoped poly-3-alkyl thiophenes electrochemically deposited on Pt as studied by NEXAFS. *Surf. Sci.* **201**, 171–184.

Treude T., Orphan V., Knittel K., Gieseke A., House C. H. and Boetius A. (2007) Consumption of methane and CO2 by methanotrophic microbial mats from gas seeps of the anoxic Black Sea. *Appl. Environ. Microbiol.* **73**, 2271–2283.

Ueno Y., Yoshioka H., Maruyama S. and Isozaki Y. (2004) Carbon isotopes and petrography of kerogens in ~3.5-Ga hydrothermal silica dikes in theNorth Pole area, Western Australia. *Geochim. Cosmochim. Acta* **68**, 573–589.

Ueno Y., Ono S., Rumble D. and Maruyama S. (2008) Quadruple sulfur isotope analysis of ca. 3.5 Ga Dresser Formation: New evidence for microbial sulfate reduction in the early Archean. *Geochim. Cosmochim. Acta* **72**, 5675–5691.

Valentine D. L., Chidthaisong A., Rice A., Reeburgh W. S. and Tyler S. C. (2004) Carbon and hydrogen isotope fractionation by moderately thermophilic methanogens. *Geochim.*

Cosmochim. Acta **68**, 1571–1590.

Valley J. W. and Kita N. T. (2009) In situ oxygen isotope geochemistry by ion microprobe. *Mineral. Assoc. Canada Short Course* **41**, 19–63.

Van Kranendonk M. J., Philippot P. and Lepot K. (2006) *The Pilbara drilling project: c. 2.72 Ga Tumbiana Formation and c. 3.49 Ga Dresser Formation, Pilbara Craton, Western Australia*., Western Australia Geological Survey, Record 2006/14, 25p.

Vandenbroucke M. and Largeau C. (2007) Kerogen origin, evolution and structure. *Org. Geochem.* **38**, 719–833.

Watanabe Y., Farquhar J. and Ohmoto H. (2009) Anomalous Fractionations of Sulfur Isotopes During Thermochemical Sulfate Reduction. *Science* **324**, 370–373. Available at: http://www.sciencemag.org/cgi/doi/10.1126/science.1169289.

Welander P. V. and Summons R. E. (2012) Discovery, taxonomic distribution, and phenotypic characterization of a gene required for 3-methylhopanoid production. *P. Natl. Acad. Sci. USA* **109**, 12905–12910. Available at: http://www.pnas.org/cgi/doi/10.1073/pnas.1208255109.

Werne J. P., Hollander D. J., Lyons T. W. and Sinninghe Damste J. S. (2004) Organic sulfur biogeochemistry: Recent advances and future research directions . *Geol. Soc. Am. Spec. Pap.* **379**, 135–150.

White A. J. R., Smith R. E., Nadoll P. and Legras M. (2014) Regional-scale Metasomatism in the Fortescue Group Volcanics, Hamersley Basin, Western Australia: Implications for Hydrothermal Ore Systems. *J. Petrol.* **55**, 977–1009. Available at: https://academic.oup.com/petrology/article-lookup/doi/10.1093/petrology/egu013.

Williford K. H., Ushikubo T., Schopf J. W., Lepot K., Kitajima K. and Valley J. W. (2013) Preservation and detection of microstructural and taxonomic correlations in the carbon isotopic compositions of individual Precambrian microfossils. *Geochim. Cosmochim. Acta* **104**, 165–182.

Williford K. H., Ushikubo T., Lepot K., Kitajima K., Hallmann C., Spicuzza M. J., Kozdon R., Eigenbrode J. L., Summons R. E. and Valley J. W. (2016) Carbon and sulfur isotopic signatures of ancient life and environment at the microbial scale: Neoarchean shales and carbonates. *Geobiology* **14**, 105–128.

Yoshiya K., Nishizawa M., Sawaki Y., Ueno Y., Komiya T., Yamada K., Yoshida N., Hirata T., Wada H. and Maruyama S. (2012) In situ iron isotope analyses of pyrite and organic carbon isotope ratios in the Fortescue Group: Metabolic variations of a Late Archean ecosystem. *Precambrian Res.* **212**–**213**, 169–193. Available at: http://dx.doi.org/10.1016/j.precamres.2012.05.003.

Zegeye A., Ona-Nguema G., Carteret C., Huguet L., Abdelmoula M. and Jorand F. (2005) Formation of Hydroxysulphate Green Rust 2 as a Single Iron(II-III) Mineral in Microbial Culture. *Geomicrobiol. J.* **22**, 389–399. Available at: http://www.tandfonline.com/doi/abs/10.1080/01490450500248960.

Zerkle A. L., Claire M. W., Domagal-Goldman S. D., Farquhar J. and Poulton S. W. (2012) A

bistable organic-rich atmosphere on the Neoarchaean Earth. *Nat. Geosci.* **5**, 359–363. Available at: http://www.nature.com/doifinder/10.1038/ngeo1425.

Zerkle A. L. and Mikhail S. (2017) The geobiological nitrogen cycle: From microbes to the mantle. *Geobiology* **15**, 343–352.

Zerkle A. L., Poulton S. W., Newton R. J., Mettam C., Claire M. W., Bekker A. and Junium C. K. (2017) Onset of the aerobic nitrogen cycle during the Great Oxidation Event. *Nature* **542**, 465–467. Available at: http://www.nature.com/articles/nature20826.

Zeyen N., Benzerara K., Li J., Groleau A., Balan E., Robert J.-L., Estève I., Tavera R., Moreira D. and López-García P. (2015) Formation of low-T hydrated silicates in modern microbialites from Mexico and implications for microbial fossilization. *Front. Earth Sci.* **3**, 1–23. Available at: http://journal.frontiersin.org/Article/10.3389/feart.2015.00064/abstract.

Zhelezinskaia I., Kaufman A. J., Farquhar J. and Cliff J. (2014) Large sulfur isotope fractionations associated with Neoarchean microbial sulfate reduction. *Science* **346**, 742–744. Available at: http://www.sciencemag.org/cgi/doi/10.1126/science.1256211.

FIGURES

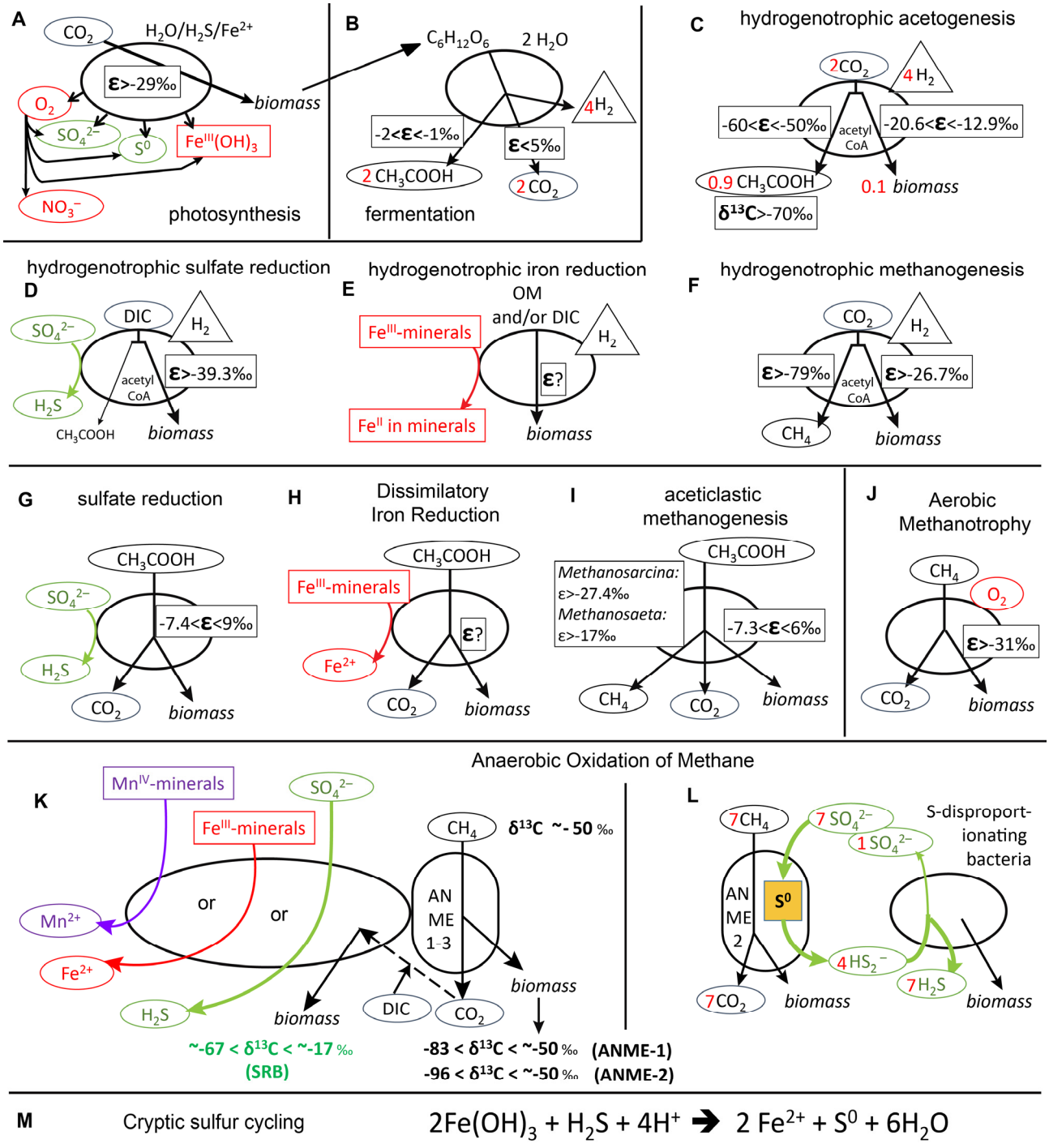

Fig. 1. Summary of the main metabolisms discussed herein. (A) Photosynthesis including anoxygenic photosynthesis oxidizing either sulfide or ferrous iron, and oxygenic photosynthesis. (B) Example of fermentation of glucose. (C-F) Hydrogenotrophic chemo(auto)trophy. DIC: dissolved inorganic carbon. (G-I) Anaerobic respiration of acetate. (J) Aerobic methanotrophy. (K-L) AOM pathways, excluding nitrate-/nitrite-dependent AOM performed by bacteria (see main text). (K) Consortia of methane-oxidizing ANME (on the right) and microorganisms that reduce sulfur, iron, or

manganese (on the left). (L) Consortia of ANME-2 that reduce sulfate to elemental sulfur and oxidize methane with S-disproportionating bacteria. (M). Cryptic sulfur cycling. Stoichiometric coefficients discussed in text appear in red. Maximum isotopic fractionations between parent carbon sources and products are indicated as ε in ‰ and maximum absolute isotopic ratios of products are indicated as $\delta^{13}C$ in ‰. References for the different panels as follows. A (Pearson, 2010). B (Penning and Conrad, 2006; Bartacek et al., 2007; Pearson, 2010; Conrad et al., 2014). C (Gelwicks et al., 1989; Preuß et al., 1989; Blaser et al., 2013; Freude and Blaser, 2016). D (Preuß et al., 1989; House et al., 2003; Londry and Des Marais, 2003). E (Zegeye et al., 2005; Roh et al., 2006; Liu et al., 2011; Etique et al., 2016). F (Botz et al., 1996; House et al., 2003). G (Londry and Des Marais, 2003; Goevert and Conrad, 2008). H (Lovley, 1991). I (Valentine et al., 2004; Penning et al., 2006; Londry et al., 2008; Goevert and Conrad, 2009). J (Summons et al., 1994; Templeton et al., 2006). K (Beal et al., 2009; Knittel and Boetius, 2009). In (K), the $\delta^{13}C$ values are given for the biomasses of microbial sulfate reducers in consortia with ANME-1 and ANME-2 methanotrophic achaea based on Orphan et al. (2002) and Treude et al. (2007), excluding two outliers with $\delta^{13}C$ values higher than that of parent methane for ANME-2 in Orphan et al. (2002). The $\delta^{13}C$ of parent methane is from Orphan et al. (2002). L (Milucka et al., 2012).

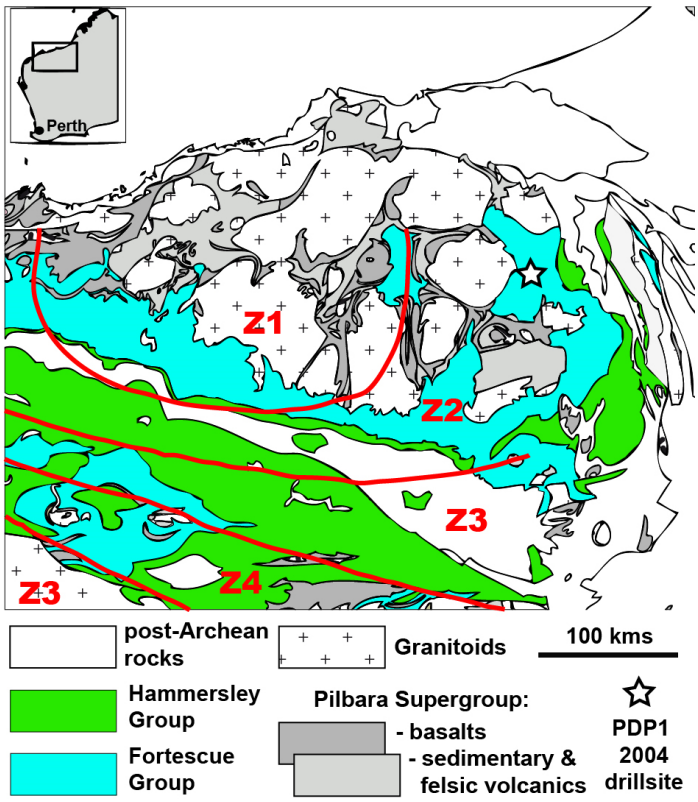

Fig. 2. Major Archean groups in the Pilbara craton and Hamersley Basin of Western Australia. Map constructed using the GeoViews.wa (https://geoview.dmp.wa.gov.au/GeoViews/) website and modified after Lepot et al. (2009a). Metamorphic zones Z1-Z4 (in red) redrawn after Smith et al. (1982). Zone Z2 corresponds to Prehnite-pumpellyite facies with epidote (Smith et al., 1982). The star indicates the locality sampled by the PDP1 drilling.

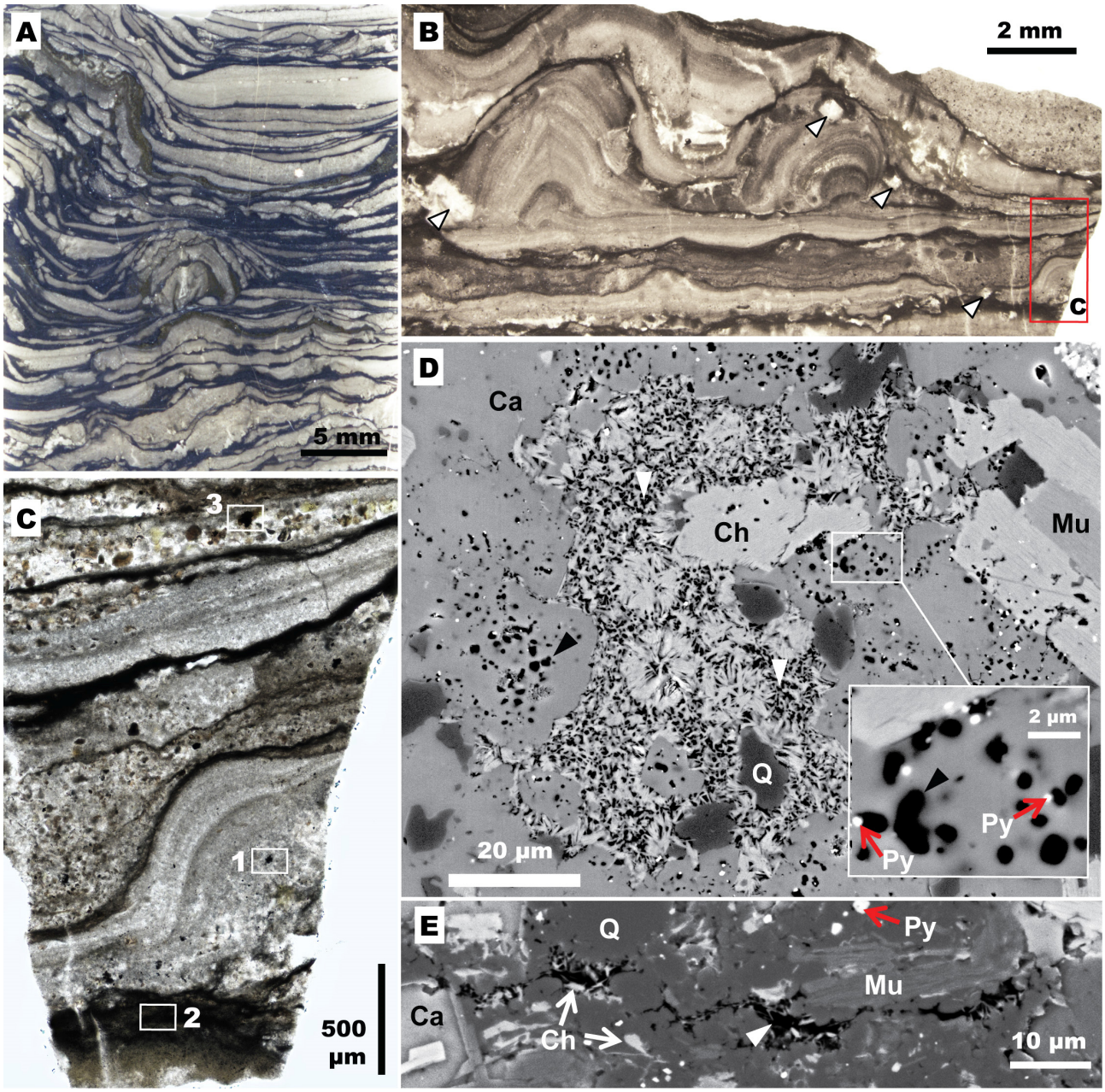

Fig. 3. Petrography of studied stromatolites. (A-C) Photomicrographs of samples KGI 68.2' (A) and 69.2a (B-C). (C) Zoom on the boxed zone in (B). Light grey layers in (A-C, box 1 in C) are dominated by micritic to microsparitic calcite. Calcite pseudomorphs after cubic halite are highlighted with arrowheads in B. Clusters of organic matter globules occur in these layers (center of box 1 in C). Black « mud-type » layers in (A-C) and box 2 in (C) are dominated by clay minerals and quartz. (Volcano)clastic grains are interspersed with micritic/microsparitic layers, and sometimes dominate these layers (e.g. box 3 in C). A large organic matter nodule appears in black in box 3 in (C). (D-E) SEM BSE images showing organic matter (black; Type A: white arrowheads, Type B: black arrowheads), quartz (Q, dark grey), muscovite (Mu, medium-dark grey), calcite (Ca, medium grey), chlorite (Ch, light grey) and pyrite (Py, white, red arrows). (D) Shows a cluster of OM embedded in

calcitic layers similar to that in box 1 in (C). Type-A organic matter occurs at the grain boundaries of chlorite, and Type B in calcite crystals (zoom in inset), sometimes with nano-pyrite. (E) Shows a mud-type layer similar to that in box 2 of (C) with a seam of Type-A organic matter associated with chlorite running through quartz.

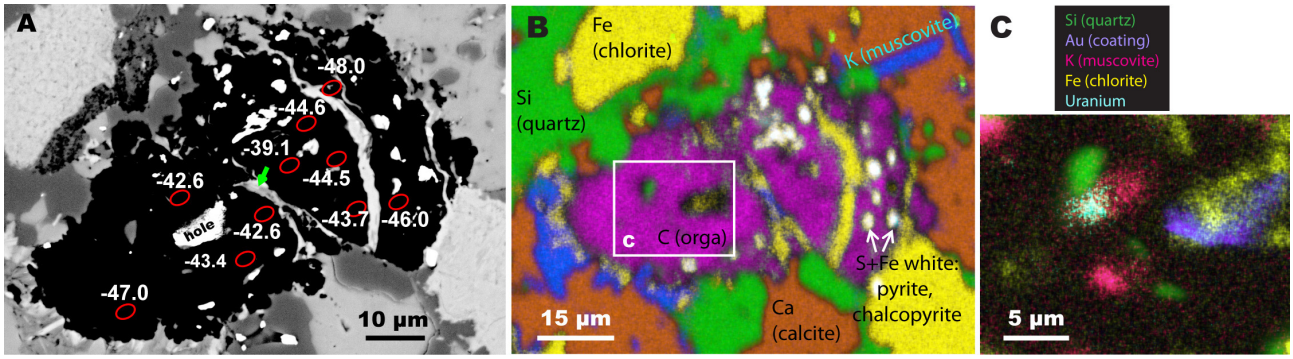

Fig. 4. Type-C organic matter nodule in sample 69.2a. (A) SEM-BSE image of a Type-C organic matter nodule in sample 69.2a located by box 3 in Fig. 3C. SIMS $\delta^{13}C_{org}$ values recorded on zones circled in red range between -39.1 and -48 ‰ ± 1.33 ‰ 2SD in this nodule and are spatially zoned. (B). SEM-EDXS map. The organic matter (pink) in the nodule is interspersed with pyrite and chalcopyrite (white) and cut across by chlorite (yellow) and muscovite (blue) microveins. (C). SEM-EDXS map of the left and central part of the nodule showing a micrometric U-rich crystal (cyan) and a hole (now filled with gold coating, purple-blue) that could correspond to a U-rich crystal removed during polishing.

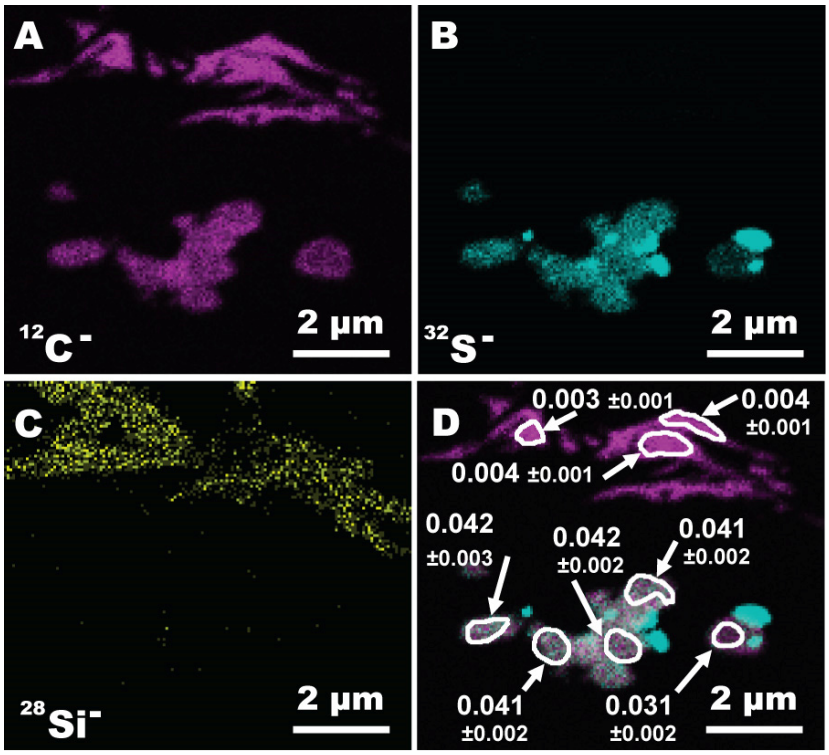

Fig. 5. NanoSIMS maps and S/C quantification in sample KGI68.2 (zone *F3*). (A-C) Single cycle maps of $^{12}C^-$ (A), $^{32}S^-$ (B) and $^{28}Si^-$ (C). The upper half of the mapped area displays Type-A OM associated with chlorite, whereas the lower half displays Type-B organic globules embedded in calcite. (D) Overlay of (A+B), where regions of interest outlined in white are associated with their atomic S/C ratios (±2SE). In (D), OM rich in organic S appears in mottled white/cyan/magenta (S: cyan + C: magenta), whereas nanopyrites appear as cyan hotspots.

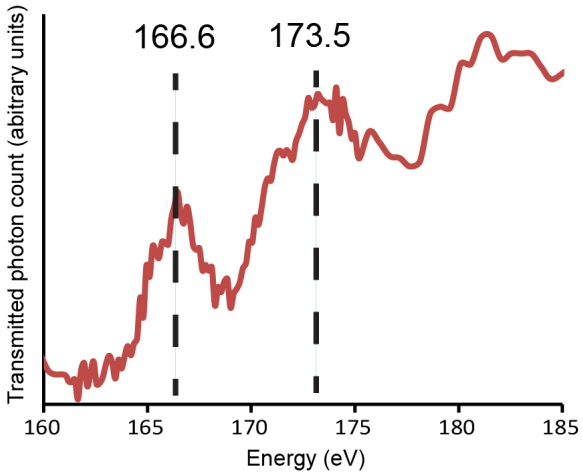

Fig. 6. Sulfur L-edge XANES spectrum of a Type-B organic globule. The sample analyzed was the globule #2 of fig. 8C of Lepot et al. (2009). Dashed lines indicate bands of thiophene groups at 166.6 and 173.5 eV (see text for interpretation).

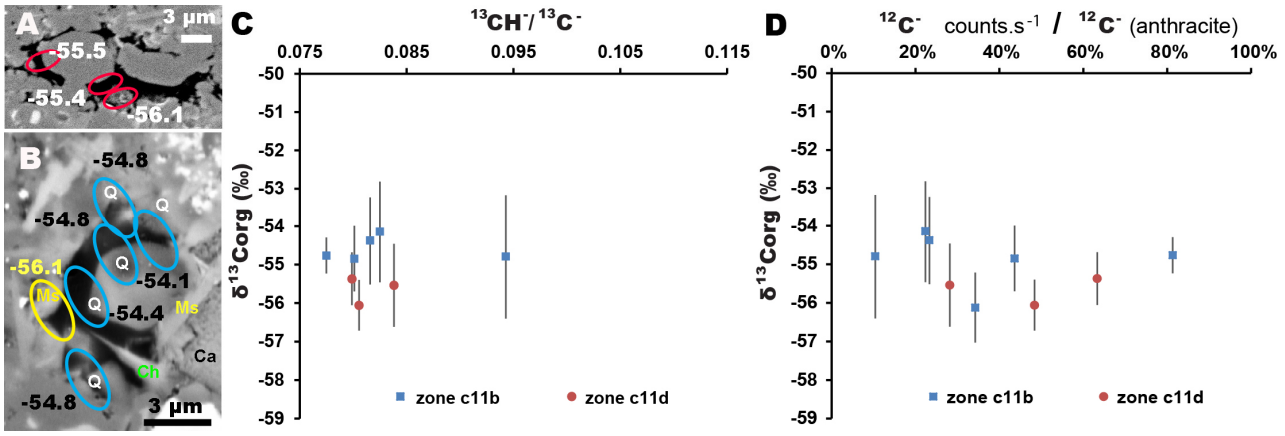

Fig. 7. SIMS analyses (3-µm spot) of Type-A organic matter in quartz. SEM BSE images of zones *c11d* (in A) and *c11b* (in B) of sample KGI68.2'. SIMS targets (circled) were chosen in order to sample zones with variable OM (in black) to quartz (in grey) concentration ratios. With the exception of one spot (yellow circle), SIMS analyses avoided crystals of muscovite (Ms, yellow) and chlorite (Ch, green) and targeted OM in quartz-only matrices. (C) In the quartz matrices (red and blue targets in A-B), the $^{13}CH^-/^{13}C^-$ ratios remain consistent with nearly all values between 0.075–0.085. The outlier has a low count rate as indicated by large 2SE error bars. (D) The $\delta^{13}C_{org}$ values are consistent and independent of the organic matter to quartz concentration ratios, which is represented here by the $^{12}C^-$ count rate in % relative to the count rate recorded on the pure anthracite bracketing standard. Error bars in (C-D) are 2SE.

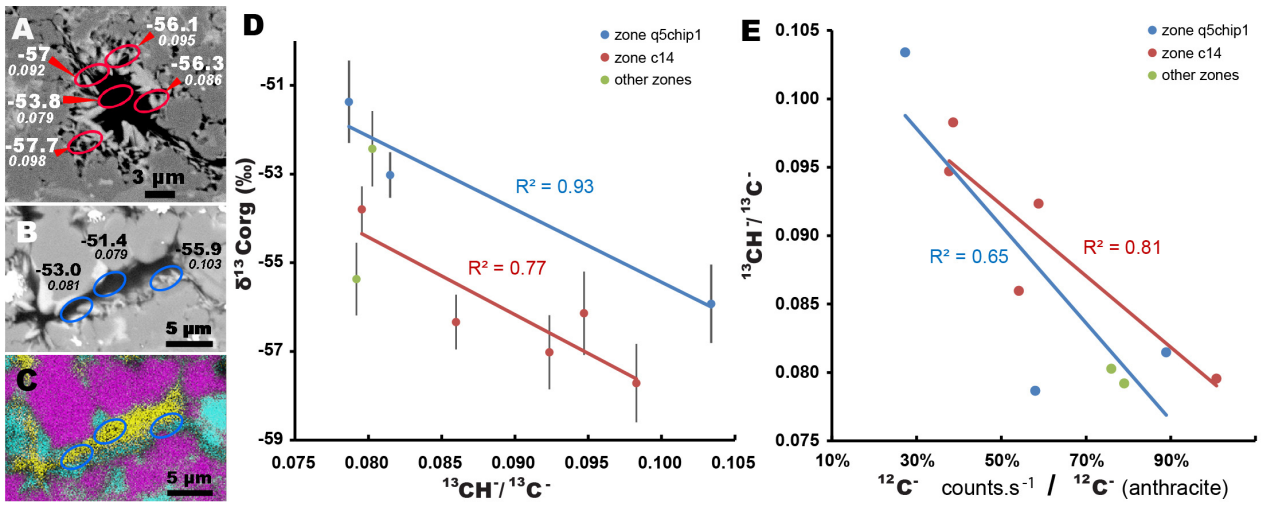

Fig. 8 SIMS analyses (3-µm spot) of Type-A organic matter in contact with chlorite±quartz. (A-B) SEM BSE images of zones *q5chip1* (A) and *c14* (B) of sample KGI68.2'. SIMS targets (circled in A-C) were chosen in order to sample zones with variable OM (in black) to chlorite (light grey to white) ± quartz (medium grey) concentrations ratios. (C) SEM-EDXS map of Si (pink, from quartz and chlorite), Al (cyan, from chlorite), and C (yellow, from OM) in the zone of (B). (D) The $^{13}CH^-/^{13}C^-$ ratios display large variations compared to those recorded in quartz as shown in Fig. 7. Linear

regressions are provided for SIMS measurements made in the same seam/cluster of organic matter. Points grouped under "other zones" are dispersed through the sample. In a given seam/cluster, $\delta^{13}C_{org}$ values decrease with increasing $^{13}CH^-/^{13}C^-$ ratios. Error bars are 2SE. (E) The $^{13}CH^-/^{13}C^-$ ratios increase at lower $^{12}C^-$ count rates that is when the organic matter to chlorite±quartz ratios decrease. The $^{12}C^-$ count rate is represented in % relative to the count rate recorded on the pure anthracite bracketing standard.

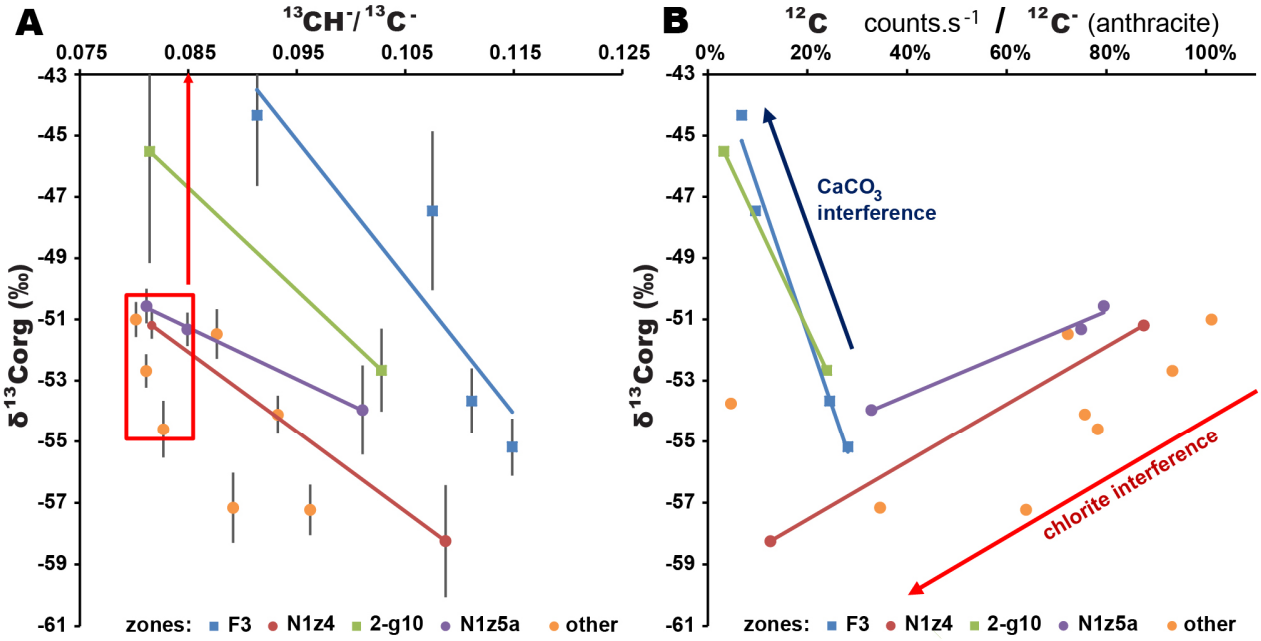

Fig. 9. SIMS analyses (1-µm spot) of Type-A organic matter in contact with chlorite and/or carbonate in sample KGI68.2 and KGI68.2'. (A) $^{13}CH^-/^{13}C^-$ ratios and $\delta^{13}C_{org}$ values (2SE error bars) display large variations comparable to those shown in Fig. 8. Linear regressions are provided for SIMS measurements made in the same seam/cluster of organic matter. Points grouped under "other zones" are dispersed through the sample. In a given seam/cluster, $\delta^{13}C_{org}$ values decreases with increasing $^{13}CH^-/^{13}C^-$ ratios. (B) In zones *N1z4* and *N1z5a*, $\delta^{13}C_{org}$ values decreases at lower $^{12}C^-$ count rates (in % relative to the $^{12}C^-$ count rate recorded on the pure anthracite bracketing standard) that is when the organic matter to chlorite±quartz ratio decreases. In contrast, in zones *F3* and *2-g10* where calcite occurred in the SIMS spots, $\delta^{13}C_{org}$ values increase with decreasing $^{12}C^-$ count rates consistent with mixing with a carbonate phase of high $\delta^{13}C_{meas}$ and low ionization yield (see text). The red box in (A) indicates analyses filtered with the criterion $^{13}CH^-/^{13}C^-$ <0.085 (see text) and not affected by carbonate interference; these analyses were recorded at high $^{12}C^-$ count rates as shown in B, hence the small error bars.

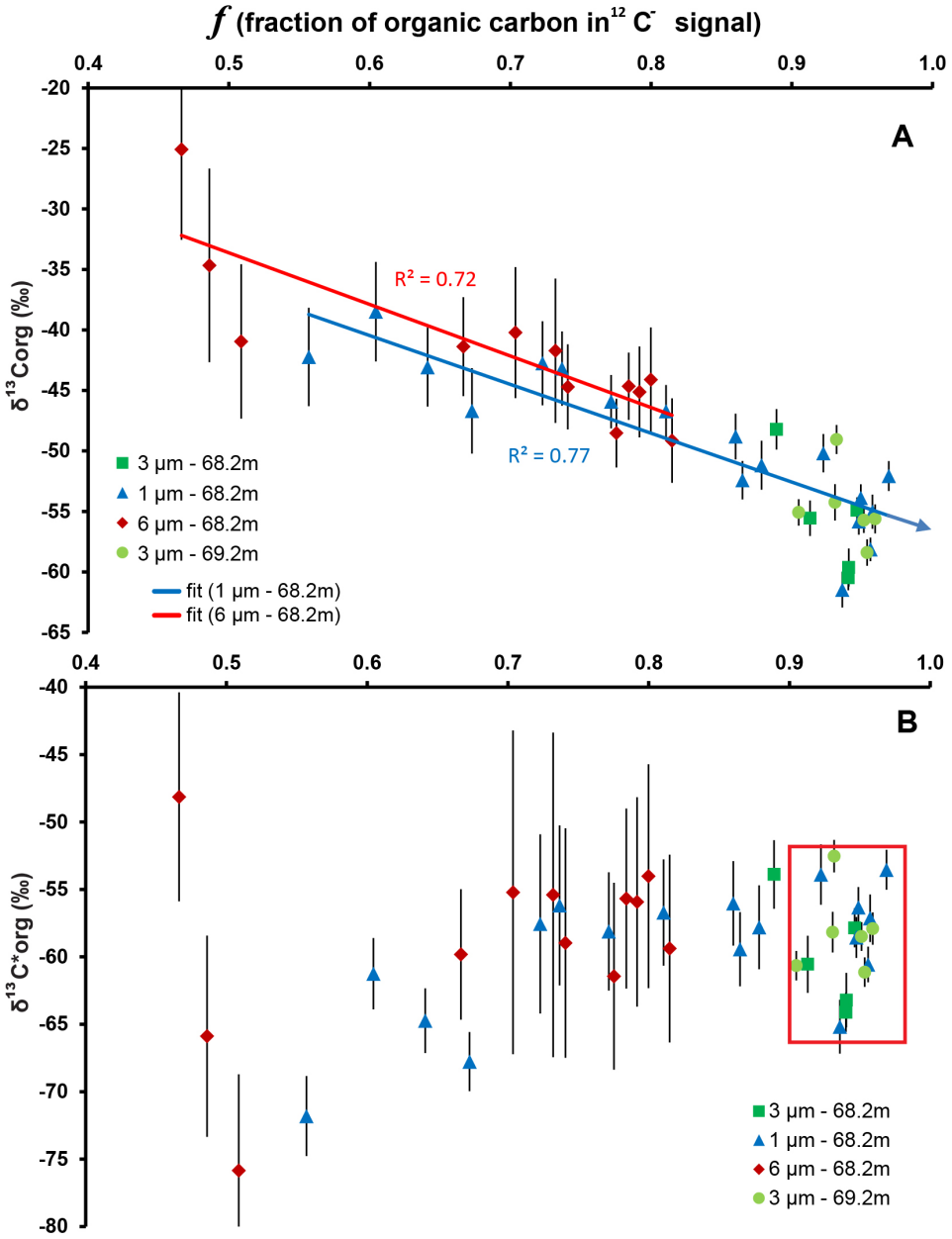

Fig. 10. SIMS analyses of micrometric Type-B organic globules in calcite crystals recorded with SIMS spot size of 1, 3 and 6 µm. (A) Plot of $\delta^{13}C_{org}$ (2SE error bars) against ***f*** (the fraction of organic C in total $^{12}C^-$ signal, see equation 10) values. The analytical sessions with 1- and 6-µm spots display a wide range of ***f*** where $\delta^{13}C_{org}$ decreases with increasing ***f***, indicating that at low OM concentrations (low ***f***), the signal contains a mixture of carbonate and organic carbons (see text). (B) Mass balance calculation (using equations 11–15) provide $\delta^{13}C^*_{org}$ values (2SE* error bars) corrected of interference of carbonate. The red box indicates the values that satisfy the filtering criterion ***f***>0.9 (see text).

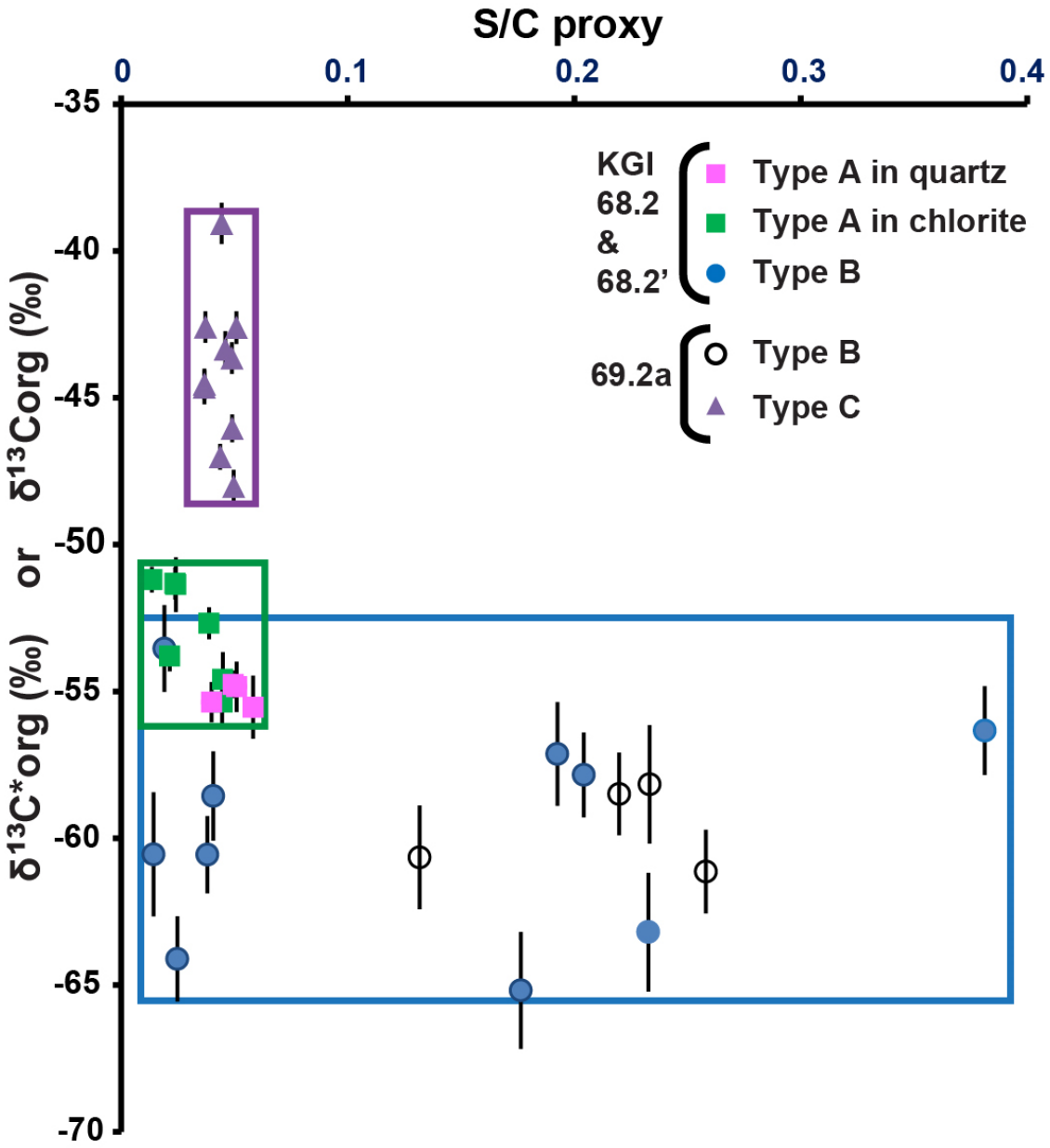

Fig. 11. Summary plot of SIMS C-isotope data and EDXS S/C semi-quantitative proxy. $\delta^{13}C^{*}_{org}$ values (with 2SE* error) are plotted for analyses corrected from carbonate interference (circles) and $\delta^{13}C_{org}$ values (with 2SE error) are plotted for all other analyses. Pink and green squares indicate values for Type-A OM in quartz and chlorite, respectively, in sample KGI68.2. Filled and empty circles indicate values for Type-B OM in samples KGI68.2 and 69.2a, respectively. Purple triangles indicate values for Type-C OM. The boxes are dimensioned to encompass the complete range of $\delta^{13}C_{org}$ and of $\delta^{13}C^{*}_{org}$ values (filtered as detailed in text) recorded in each OM type (green: A, blue: B, purple: C) including those SIMS spots where S/C semi-quantifications were not available.